NTNU

Norwegian University of
Science and Technology

Intraoperative Ultrasound Strain Imaging of Brain Tumors

Thomas Kristoffersen Børstad

Master of Science in Engineering Cybernetics
Submission date: June 2011
Supervisor: Hans Torp, ITK
Co-supervisor: Tormod Selbekk, Sintef

Norwegian University of Science and Technology
Department of Engineering Cybernetics

Forord

I skrivende stund er klokken 23:06, datoen er 20. juni 2011 og det er nøyaktig 56 minutter til denne masteroppgaven skal leveres. I motsetning til hvordan leseren antakelig tolker dette, så er denne oppgaven et resultat av et halvt år med mye jobbing.

Jeg vil gjerne benytte anledningen til å takke min hovedveileder, professor Hans Torp ved Institutt for sirkulasjon og bildediagnostikk. Hans har vært til svært god hjelp både gjennom prosjekt- og masteroppgaven, og har med et uvanlig godt humør alltid kunnet oppklare de spørsmålene jeg måtte ha omkring ultralyd signalbehandling.

Samtidig vil jeg takke min biveileder Tormod Selbekk fra Sintef, avdeling for medisinsk teknologi. Tormods tidligere arbeid har dannet grunnlaget for denne masteroppgaven, og han har introdusert meg til den kliniske bruken av ultralyd på hjernen. Tormod har også lært meg alt det jeg kan om hjernesvulster.

Det som kommer til å stå igjen som den sterkeste, og mest spennende, opplevelsen fra dette arbeidet er utvilsomt det å ha fått væe med å obsevere under en hjerneoperasjon. Det har vært en drivkraft bak hele min masteroppgave, og var nok ikke noe jeg hadde forventet å oppleve gjennom mitt studium på NTNU, da jeg begynte som førsteårs student i 2006.

Til slutt fortjener min far, Kjell Kristoffersen, takk for nyttige innspill med jevne mellomrom. Antakelig må nok han også ta litt av skylden for at jeg skrev en masteroppave om ultralyd.

Summary

Intraoperative ultrasound strain imaging of the brain visualizes brain tissue deformation as an image. The hypothesis is that strain and elastographic values can be used to complement conventional B-mode image in the task of brain tumor segmentation. A key assumption is that the natural pulsation of the cerebral arteries causes deformation in the brain tissue that is measurable with ultrasound.

Strain values are found with a least-squares technique that estimates the spatial derivative of axial velocity, which in turn is measured using a phase-based velocity estimator. A correlation coefficient is calculated for each estimate, giving an indicator of estimation accuracy. Additionally a method for hiding estimates of bad quality based on correlation coefficient thresholding is demonstrated. Moreover, a novel elastographic processing technique suitable for cineloop display is introduced. This method extracts a stiffness parameter from a series of strain images, producing an elastogram. A graphical user interface allowing the user to change parameters and see the corresponding result in real-time, minimizing the time needed for parameter optimization, has been developed.

The method has been tested using an elasticity phantom. The phantom elastogram cineloop shows a live image that visualizes the difference between stiff and soft tissue well, portraying information not found in the B-mode image. The conclusion is that the proposed elastographic technique, combined with correlation coefficient thresholding, produces elastograms that are suitable for real-time display. This technique is not limited to imaging of the brain, and could, with different parameters, be used for imaging other parts of the body as well.

Clinical data sets from two brain tumor patients have been studied as well, where the estimated velocity, strain and elastographic values is discussed in detail. In both patients the tissue movement due to arterial pulsation was measurable with ultrasound. For one patient, a correlation was found between tissue pathology and estimated strain and elastographic values. For the second patient the strain and elastographic processing broke down, and no similar correlation was found.

Contents

CHAPTER 1

Intraoperative ultrasound

Ultrasound is one of the major medical imaging modalities, with clinical applications in many fields of medicine. Compared to other modalities such as MRI or CT, ultrasound has several advantages such as the portability of the scanner, low cost, and the ability to provide real-time imaging. Ultrasound emits no ionizing radiation and, together with MRI, is considered as one of the safest modalities. Drawbacks includes a small field of view, the difficulty of imaging through bone and similar structures, and the high attenuation of ultrasound waves in tissue. In general this means that the image quality can vary between patients and is influenced by the skill of the sonographer.

Most people probably know ultrasound from its use in *obstetrics* (the medical field dealing with child birth), where scanners are used to image the fetus during pregnancy. However ultrasound is used in a number of different clinical settings, such as *cardiovascular* (heart and blood vessels), *gastroenterology* (digestive system) and *urology* (urinary tracts and reproductive system).

The use of ultrasound in *neurology* (nervous system), more specifically ultrasound imaging of the brain, has received relatively little attention. The reason for this is that the brain is surrounded by bone, which reflects most of the incoming ultrasound waves, which makes imaging difficult. Nevertheless, by taking advantage of the thinner areas of the skull and restricting imaging to only measure blood flow, a method known as transcranial Doppler ultrasound (Markus, 2000) is used non-invasively on the brain. Transcranial sonography (Meyer-Wiethe et al., 2009) and transcranial tumor ablation (Jagannathan et al., 2009) are other ultrasound techniques which have been used on the intact skull, with varying degree of success.

If a brain tumor is to be removed surgically, a part of the scull is temporarily removed (a procedure known as a *craniotomy*) to give the surgeon access to the brain. By using ultrasound during such a surgery, the brain can be imaged directly through the hole in the skull, giving much better imaging conditions. The surgical removal of a tumor is a complex procedure which deserves to be studied in more detail. What follows is an explanation of some of the typical clinical steps a brain tumor patient at St. Olavs hospital (Trondheim, Norway) will go through.

1.1 Surgical removal of brain tumors

What is a tumor?

A tumor is an abnormal collection of tissue caused by excessive cell growth. If the tumor is *malignant* (as opposed to *benign*), there is a serious health risk to the patient which might ultimately lead to the death of the patient. A malignant tumor is likely to grow uncontrollably, or spread (*metastasize*) to other parts of the body, though it is rare that a tumor which originates in the brain to metastasize. A brain tumor is thus a tumor located in the brain.

A brain tumor patient's symptoms can range from no symptoms at all, to degraded memory, speech impediments, worsening of motor function or other neurological conditions. In general brain tumors affects each patient differently, depending on the location, size and type of tumor. If a patient is suspected to have a brain tumor, the patient will typically be scheduled for an MRI brain scan.

An initial MRI brain scan

The MRI scan provides an excellent anatomical view of the brain, and is of great help when determining the position and size of the tumor, as the tumor is often easily distinguishable in the image. An MR image from a tumor patient is shown in Fig. 1.1, where even for the untrained eye it is easy to see that there is an abnormality.

For some patients the best treatment is to physically remove the tumor, or parts of it, through surgery. If the medical team decides that the tumor should be surgically removed, the team will first try to define the borders of the tumor as good as possible based on the MR images. It is important to locate critical nearby neurological paths and structures that must not be damaged during surgery, a task which might require new scans such as functional MRI (fMRI) or diffusion tensor imaging (DTI). These kind of

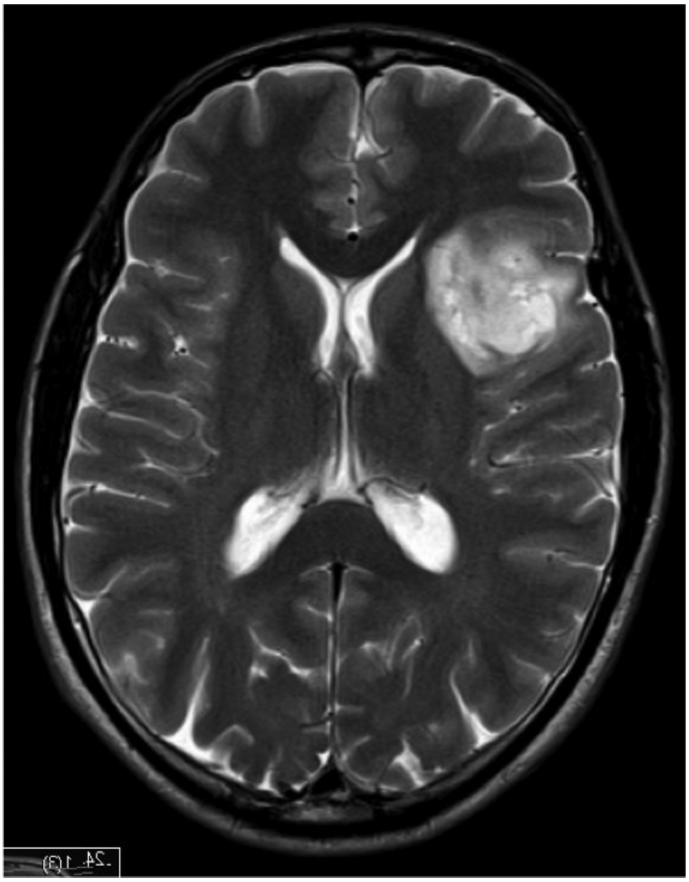

Figure 1.1: Preoperative MR image of a tumor patient. The tumor is visible in the upper right quadrant of the brain.

scans provides the surgeon with more information than the anatomical MR image alone.

A key step in the pre-surgical planning is the decision on *how* to reach the tumor, with the goal of doing as little damage to healthy tissue as possible. Of course none of these steps are an exact science and every case is unique, thus it is important that the team has good enough images on which they base their decision.

Navigated neurosurgery

With the preoperative planning finished, the neurosurgery is scheduled. New MR images are taken the day before surgery, with parameters optimized to provide images that are fed to a navigational system which is used

during surgery. A new brain scan also gives as up-to-date information as possible, which could be important since tumor might have changed in size since the initial MR scan.

During surgery, the surgeon uses the MR images as a guide to locate the tumor and important neurological structures, much like a conventional map is used to navigate in terrain. To assist the surgeon with this task, a multimodal neuronavigation system SonoWand (Sonowand AS, Trondheim, Norway) is used. The SonoWand system enables the surgeon to physically point (using a pointer tool) anywhere on, or inside, the patient's brain and the system will mark the same point in the MR image. This is illustrated in Fig. 1.2. The system has the ability to do 3D ultrasound recordings during surgery, and these recordings can be used for navigation in the same way as the MR images are used. A screenshot from the system, when using both MRI and US images for navigation, is shown in Fig. 1.3.

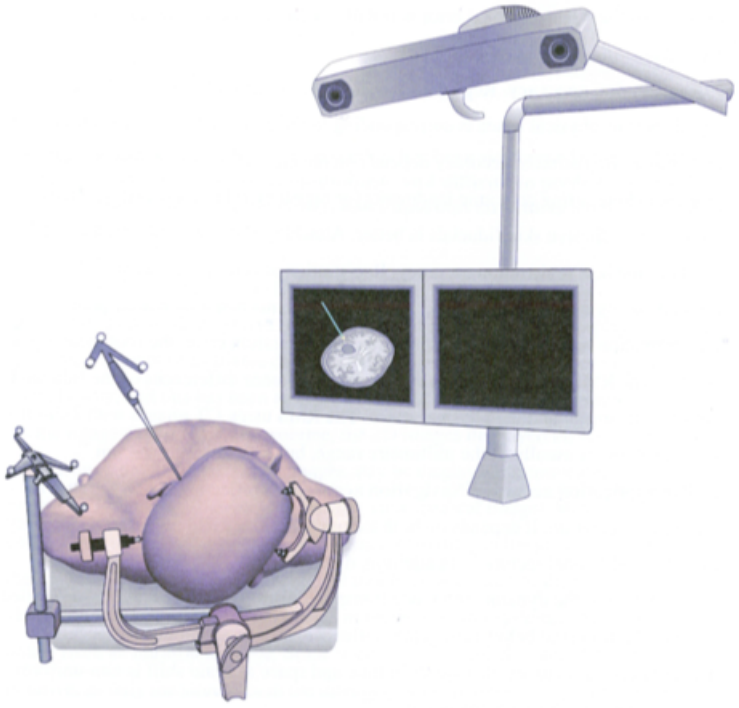

Figure 1.2: The SonoWand system shown together with the pointer tool used for navigation. Image courtesy of (Rygh, 2008)

The motivation behind using ultrasound in addition to MRI is to get real-time information along with the ongoing surgical resection. Just the

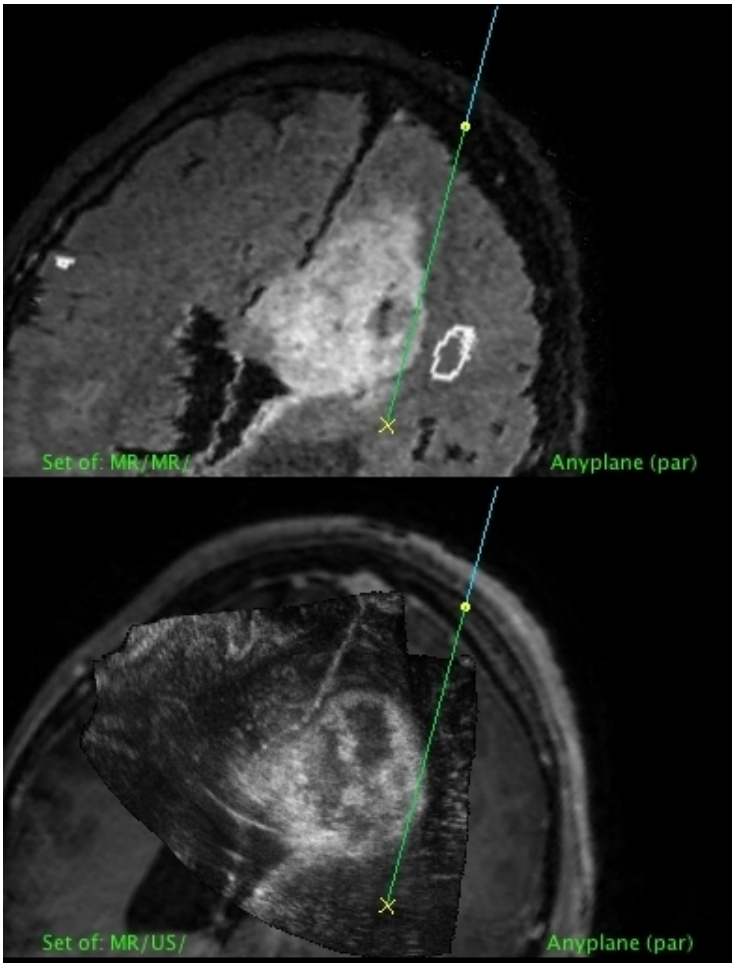

Figure 1.3: Screenshot from the SonoWand system. The upper image shows the preoperative MR scan, while the lower image shows intraoperative US superimposed on the MR image.

fact that the patient might be lying in a different position than during the MR recordings, can make the brain move with respect to the skull, causing the MR "map" to be inaccurate.

Further more the craniotomy can cause the brain to shift, causing discrepancies compared with the preoperative images.The combination of such accuracy-decreasing effects occurring due to the brain moving or changing shape is known as *brain shift*. The advantage of using ultrasound is that it is not affected by brain shift, since new recordings can be made at any time. Naturally as more and more of tumor is removed the validity of the

preoperative images decreases as well.

An ultrasound recording is usually made after the craniotomy, but before the resection is started. The probe, covered in sterile draping filled with acoustic gel, is placed directly on the *dura mater*. This allows the surgeon to recognize for any brain shift that may have occurred. As the surgery continues, the surgeon will periodically use ultrasound to monitor the degree of tumor removal and to locate and avoid critical neurological structures.

Finally, shortly after surgery the patient will undergo a new MRI scan, so that the result of the operation can be assessed.

1.2 Ultrasound based tumor segmentation

Perhaps needless to say by now, brain surgery is a complex procedure where a great deal of responsibility lies in the hands of the neurosurgeon. Thus it is important that the surgeon is able to separate between tumorous tissue which should be removed, and healthy tissue which should be left untouched. The clinical usefulness of intraoperative ultrasound in this kind of surgery is thus dependent on the ability to successfully separate between tumor tissue and healthy tissue.

For some patients, the tumor is clearly visible on the conventional ultrasound B-mode image, an example being the tumor already depicted in Fig. 1.3. In other cases however, it may not be possible to clearly identify the tumor borders from the B-mode image. This is seen in Fig. 4.13, on page 48, where the separation between tumorous and healthy tissue is not possible from B-mode alone. A good discussion on the challenges of using B-mode during brain tumor surgery, and how such challenges are related to the outcome of the operation, can be found in (Solheim et al., 2010). Such difficulties makes it natural to investigate if other ultrasound techniques can complement B-mode with respect to tumor segmentation, and has been the motivation behind this thesis.

1.3 Goal of thesis

The normal B-mode image shows the strength of the ultrasound signal that is echoed back from the tissue when the tissue is insonated. Using signal processing other quantities than echo strength, such as for example flow velocity, can be imaged. A technique known as *strain imaging* attempts to image the amount of compression in the tissue, which again can be related to tissue stiffness.

Knowing that tumors in general are stiffer than healthy tissue (Souchon et al., 2003; McKnight et al., 2002), and that tissue stiffness in general is uncorrelated with echo strength (Ophir et al., 1999), it is reasonable to believe that strain imaging could potentially be used to complement B-mode in the task of tumor segmentation. This idea is the key motivation behind this Master's thesis. Initial results on the topic has been published by my co-advisor Tormod Selbekk, in (Selbekk et al., 2005) and (Selbekk et al., 2010).

This thesis builds upon preliminary work, a "Master's project", done by the author in the fall of 2010. The project studied different axial velocity estimators for use in strain estimation of the brain (Boerstad, 2010). Three key issues were identified during the course of the project work, and these issues serve as the primary goal of this thesis:

1. It was found that image quality varied significantly with change of the estimation parameters. Manually tuning parameters to achieve better results was cumbersome, and there was no guarantee that good parameters for one data set could be used successfully on another. **Thus a method to quickly and intuitively optimize algorithmic parameters is desired**

2. It was difficult to separate between "true" strain and elastographic estimates, and estimates that were simply a result of noise. **We need a way to better evaluate if the estimated values are just a result of noise, or if they represent actual elastic properties**

3. The methods were only tested on simulations and on phantom data. A natural next step was to study the results from the estimators on clinical data. **We want to study if there is any relationship between the pathology of the tissue and the estimated strain and elastographic quantities.**

1.4 Structure of thesis

Chapter 2 deals with the theory behind the velocity, strain and elastographic estimators. Then chapter 3 presents a MATLAB graphical user interface that allows for fast, manual optimization of algorithmic parameters, together with a presentation of the ultrasound scanners and elastographic phantom used in this thesis. Finally the pulsation of the carotid artery is studied.

The following chapter 4 shows algorithmic results, based on an elastographic phantom, and clinical results from two brain tumor patients. The results and findings are then discussed in detail in chapter 4. Finally chapter 5 provides a conclusion, together with suggestions for future work.

In addition to these chapters, appendix A contains the key parts of the estimation source code, appendix B an ad hoc description of how to tune parameters, and appendix C contains the algorithmic and acquisition parameters used to generate all results.

CHAPTER 2

Theory

Imaging tissue stiffness using ultrasound is often referred to as *elastography*, a term first introduced by (Ophir et al., 1991). The term was used to describe a method where the local axial strain distribution in tissue, caused by an externally applied force, was estimated using ultrasound. Since the term was originally coined, elastography has become an umbrella term to cover a wide variety of modalities that image elastic properties in tissue.

Today most of the literature reserve the term elastography for techniques which image true elastic properties such as Young's modulus. Nevertheless it is common to find papers which present strain images and name them *elastograms*, which can lead to a confusing mix of terminology. In this thesis the term *strain imaging* is used when talking about imaging axial strain, while elastography is reserved for the post-processed image which attempts to give a better indication of relative tissue stiffness. The image that this processing produces is the elastogram.

A key difference from the setup originally used by Ophir, is that we do not use an externally controlled force to cause compression. Instead we rely on the natural pulsation of the arteries to cause tissue deformation, and measure the strain this pulsation causes. This means that we have do not control the strain-generating force, which is a significant challenge and is discussed in more detail later. The fundamental signal processing we use however, is based on the same general idea of Ophir.

The major steps in the elastographic signal chain are velocity estimation, followed by strain estimation, followed by elastographic processing. Note that since the project (Boerstad, 2010) covered the velocity estimation step in detail, only a brief summary will be presented here.

2.1 The two-dimensional autocorrelation function

The following section on mathematical notation is copied directly from (Boerstad, 2010), with a slight change of notation for consistency:

”Assume that the RF signal data available consists of **M** depth samples, **N** scan lines and **O** frames. The RF data can be represented as a real, 3-dimensional signal $x[m, n, o]$, with the lower-case indexes m, n, o representing the depth, scan line and frame number respectively. The depth samples m are ordered increasingly with distance from the transducer, the scan lines n from left to right according to the image displayed on the screen, and the frames o ordered increasingly with time of acquisition.

The *analytical signal* $x_+[m, n, o]$ is then defined as:

$$x_+[m, n, o] = x[m, n, o] + \mathrm{i} \cdot \mathcal{H}\{x[m, n, o]\} \tag{2.1}$$

where $\mathcal{H}\{\cdot\}$ represents the 1D Hilbert transform along the depth dimension of the signal.”

The 2D autocorrelation estimate of x_+ at lag $[u, v]$, at a fixed point in space-time given by $[m, n, o]$ is defined as

$$\gamma'[u, v; m, n, o] = \sum_{i=m-\lfloor(\mathbf{U}-1)/2\rfloor}^{m+\lceil(\mathbf{U}-1)/2\rceil} \sum_{k=o}^{o+\mathbf{V}-v-1} x_+[i, n, k] x_+^*[i+u, n, k+v] \tag{2.2}$$

with * denoting complex conjugation. Using the same terminology as (Loupas et al., 1995), the parameter $\mathbf{U} \geq 1$ is known as the *range gate* while $\mathbf{V} \geq 2$ is known as the *ensemble length*. While Loupas presents an autocorrelation estimate based on a single range gate and pulse ensemble, Eq (2.2) represents how to apply Loupas' idea to a 3-dimensional dataset. In fact Eq. (11) in (Loupas et al., 1995) is a special case of Eq. (2.2), with range gate equal to the number of samples ($\mathbf{U} = \mathbf{M}$).

Eq. (2.2) can be extended to also include samples from **N** scan lines, with $\mathbf{N} \geq 1$, in an attempt to get a a more accurate autocorrelation estimate at the cost of lower lateral resolution. Then the autocorrelation function becomes

$$\gamma[u, v; m, n, o] = \sum_{j=n-\lfloor(\mathbf{N}-1)/2\rfloor}^{n+\lceil(\mathbf{N}-1)/2\rceil} \gamma'[u, v; m, j, o] \tag{2.3}$$

2.2 The 2D-AC and 1D-AC axial velocity estimators

The first step in the signal chain is the estimation of the velocity along the ultrasonic scan lines, i.e the axial velocity. For an explanation of the physical situation, and the derivation of phase-based velocity estimators, see (Boerstad, 2010).

Any fundamental book on ultrasound contains a discussion on the Doppler effect, together with the Doppler equation

$$f = \frac{2v_a}{c} f_0 \tag{2.4}$$

with f being the frequency shift seen by an observer standing at the point of origin, of an echoed wave with frequency f_0, v_a is the axial velocity of the object reflecting the wave, and c is the speed of sound. The shift in frequency is known as the *Doppler effect*. Pulsed based methods actually do *not* make use of the Doppler effect (Jensen, 1996), but Eq. (2.4) is still valid, but with slightly different meaning. The frequency f now denote the frequency of the signal resulting from sampling a sequence of pulse returns at a constant depth. Rearranging Eq. (2.4), we can solve for axial velocity to get

$$v_a = \frac{c}{2} \frac{f}{f_0} \tag{2.5}$$

Now from (Barber et al., 1985) an estimate for the frequency f can found using the autocorrelation function by

$$\hat{f} = \frac{1}{2\pi} \frac{\arg\{\gamma[0,1]\}}{\mathrm{T_{PR}}} \tag{2.6}$$

with T_{PR} being the time between pulse returns, and having omitted the specific space-time location $[m, n, o]$ for simplicity. By combining Eq. (2.5) and Eq. (2.6) we get the 1D-AC axial velocity estimator

$$\hat{v}_a = \frac{c}{2(2\pi f_0)} \frac{\arg\{\gamma[0,1]\}}{\mathrm{T_{PR}}} \tag{2.7}$$

The term 1D is used because the autocorrelation function $\gamma[u, v]$ is only evaluated at one lag along a single dimension.

Using a similar idea to Barber, (Loupas et al., 1995) showed that the center frequency f_0 of the imaging pulse could be estimated as

$$\hat{f}_0 = \frac{1}{2\pi} \frac{\arg\{\gamma[1,0]\}}{\mathrm{T_s}} \tag{2.8}$$

with T_s being the time between depth samples. By combining this result with the 1D-AC estimator, a new estimator emerges as

$$\hat{v}_a = \frac{c}{2}\frac{\mathrm{T_s}}{\mathrm{T_{PR}}}\frac{\arg\{\gamma[0,1]\}}{\arg\{\gamma[1,0]\}} \tag{2.9}$$

which is known as the 2D-AC estimator.

The correlation coefficient as an estimation quality indicator

A correlation coefficient is a ratio that measures the degree of correlation between two signals. We define the correlation coefficient (c) as the magnitude of the ratio of the autocorrelation at one slow-time lag over the autocorrelation at zero lag

$$c = \frac{\mathbf{O}}{\mathbf{O}-1} \cdot \left|\frac{\gamma[0,1]}{\gamma[0,0]}\right| \tag{2.10}$$

where the scaling factor is needed because the no-lag estimate $\gamma[0,0]$ involves one extra correlation-pair matrix compared with $\gamma[0,1]$. The scaling factor ensures that $c = 1$ if the RF-signal matrices are stationary, and decreases towards zero with increasing signal decorrelation.

The signal to noise ratio (SNR) of velocity estimates is known to increase with an increasing correlation coefficient (Souchon et al., 2003), meaning that the correlation coefficient can be used as an indicator of the quality of the estimates.

2.3 Strain and elastic parameters

Formally, the strain ε of an object that has been deformed along one axis is defined as the quantity:

$$\varepsilon = \frac{\Delta L}{L_0} = \frac{l - L_0}{L_0} \tag{2.11}$$

with ΔL being the difference between the final length l of the object and the pre-deformation length L_0. The quantity ε is also sometimes known as the *engineering* strain or *Cauchy* strain.

It is important to note that strain is not a true elastic property of a material, a strain value by itself is not a parameter that quantitatively characterizes an object. This is because the amount of deformation ΔL,

and thus the strain, is dependent on the stiffness of the object *and* the force that caused the compression. The relationship between deformation, applied force and stiffness of an object is well known to most engineers, it is Hooke's law

$$F = -kx \tag{2.12}$$

where F is the force needed to compress a uniform object by a length x from its initial length, with the object having a spring constant (stiffness) k. If we divide both sides of Eq. (2.12) by the cross sectional area A_0 that the force is acting on, while using the definition *stress* as $\sigma = F/A_0$, we get

$$\begin{aligned} \sigma &= -\frac{k}{A_0}x \\ &= \frac{-kL_0}{A_0}\frac{x}{L_0} \\ &= E\,\varepsilon \end{aligned} \tag{2.13}$$

where E is the elastic property known as Young's modulus, which is a true *material* property. For so-called linear-elastic materials Young's modulus is constant over wide range of stress-strain values, giving a linear relationship between stress and strain. Unfortunately, from in-vitro research done on swine brains (Miller and Chinzei, 1997, 2002), the Young's modulus in brain tissue has been shown to vary significantly with a change in the stress-strain relationship. The researchers conclude: "The stress-strain curves are concave upward for all compression rates containing no linear portion from which a meaningful elastic modulus might be determined." (Miller and Chinzei, 1997). This makes it difficult to characterize brain tissue even knowing the Young's modulus, without additional information about stress or strain.

Despite the limitations, quantifying tissue strain could still potentially provide clinically useful information due to the fact that

- If a tissue region is compressed by a uniform force, the strain distribution in the tissue will vary with the stiffness of the different tissue regions.
- If the compression is caused by an internal force, such as natural pulsation, abnormal strain values could potentially indicate a pathological condition.

To determine if natural pulsation strain imaging of the brain could aid with tumor segmentation, it is natural to investigate if there is a statistical

difference in strain values from tumors versus strain values from normal tissue. If such a relationship can be shown consistently across different patients, then the clinical usefulness of strain imaging could be shown without making assumptions about stress distribution or Young's modulus.

Generating tissue deformation

From Eq. (2.13) it is seen that for there to be any strain at all, the tissue needs to be put under some form of mechanical stress. In other parts of the human body, research groups have relied on several different mechanism to generate this stress, including a freehand technique (Shiina et al., 2003; Hall et al., 2003), natural pulsation of arteries (Dighe et al., 2008; Cespedes et al., 2000), the expansion/contraction of the heart (Heimdal et al., 1998), using ultrasonic compression techniques (shear waves or acoustic radiation pressuse) (Bercoff et al., 2004; Nightingale et al., 2002) or using a vibrating mechanical actuator (*vibrography*) (Pesavento et al., 2000).

In intraoperative ultrasound strain imaging of the brain, the methods presented in literature have been natural pulsation (Selbekk et al., 2005, 2010), freehand palpation (Uff et al., 2009) and vibrography (Scholz et al., 2005, 2007). A recent article has also looked at using shear waves to map elasticity in animal brains (Mace et al., 2011), an interesting technique with obvious potential to be used on the human brain as well.

This clinical strain images presented in this thesis have all relied on natural pulsation of the arteries to generate strain. The reasoning behind this is because this eliminates the need to externally apply any deformation to the brain, avoiding any possible side effects such external deformation might cause (if any). The data sets used for strain processing are the same ones that are already being recorded to do conventional B-mode imaging, meaning that the imaging set-up does not have to be changed.

2.4 Velocity based strain estimation

If the local echo delay that occurs between a pre- and post-compression scan line is known, then the axial strain of a segment of length Δz is (Cobbold, 2007, page 563)

$$\varepsilon = \frac{c_0}{2\Delta z}(\tau_l - \tau_u) \tag{2.14}$$

with τ_l and τ_u denoting the echo delay at the lower (furthest away from the transducer) and upper endpoint of the segment respectively. The velocity

matrix $\hat{V}[m,n]$ is proportional to the local delays

$$\hat{\tau}[m,n] = \frac{2\,\mathrm{T_{PR}}}{c_0}\hat{V}[m,n] \tag{2.15}$$

with $\mathrm{T_{PR}}$ being the time between the pulse returns.

We now considerer an axial segment along a single scan line. Let the segment be centered at depth m, with the end points at $m_l = m + \lceil \Delta m/2 \rceil$ and $m_u = m - \lfloor \Delta m/2 \rfloor$, with Δm is the total number of samples from the segment. The tunable parameter Δm thus controls the length of the axial segment, with the relationship

$$\Delta z = \Delta m\,\mathrm{T_s}\frac{c_0}{2} \tag{2.16}$$

where $\mathrm{T_s}$ is the RF sampling period.

Central Difference Strain Estimation

We can combine the three equations, eq. (2.14), eq. (2.15) and eq. (2.16), and define the local axial strain matrix as

$$\hat{\varepsilon}[m,n] = \kappa \cdot \frac{\hat{V}[m_l,n] - \hat{V}[m_u,n]}{\Delta m} \tag{2.17}$$

using the definition $\kappa = 2\,T_{PR}\,/\,(c_0 T_s)$. The fractional term in Eq. (2.17) represents the numerical differentiation of $\hat{V}[m,n]$ in the axial direction, with axial length Δm. From the theory of finite differences we recognize the numerator term (if Δm is even) as the *central difference* formula. We thus name Eq. (2.17) *the central difference strain estimator*. This was the estimator that was used in (Boerstad, 2010).

Least-squares Strain Estimation

We recognize the central difference estimate in Eq. (2.17) as the slope of the straight line that goes through the velocity estimates $\hat{V}[m_l,n]$ and $\hat{V}[m_u,n]$, scaled by κ. In the preliminary project (Boerstad, 2010) it was found that an axial segment length corresponding to a $\Delta m = 90$, or 3.465 mm, gave good results for the phantom data. With central difference estimation only the velocity samples from the endpoints m_l and m_u are used, while the samples located in the interior of the segments are discarded. A natural idea is to include these interior estimates when estimating the velocity slope as well. This can be done by using classical least-squares line fitting.

Since we only estimate axial strain, we can limit ourselves to study the velocity vector $v[m]$ from a single axial segment, where the segment is centered at depth m and length given by Δm. Assuming that velocity is linear with depth, which is equivalent to assuming linear elasticity, within the segment we can write the relationship

$$v[m] = a \cdot m + b \tag{2.18}$$

where the index m is a natural number restricted by $m_u \leq m \leq m_l$. The strain in this segment is then given by $\varepsilon_m = a \cdot \kappa$. We can reformulate Eq. (2.18) into matrix form as

$$\begin{bmatrix} v[m_u] \\ v[m_u+1] \\ v[m_u+2] \\ \vdots \\ v[m_l] \end{bmatrix} = \begin{bmatrix} m_u & 1 \\ m_u+1 & 1 \\ m_u+2 & 1 \\ \vdots & \vdots \\ m_l & 1 \end{bmatrix} \begin{bmatrix} a \\ b \end{bmatrix} \tag{2.19}$$

and by using compact notation as

$$\mathbf{v} = \mathbf{A} \begin{bmatrix} a \\ b \end{bmatrix} \tag{2.20}$$

Instead of the true velocity vector $\mathbf{v}$, only the inaccurate (noisy) measurement vector $\hat{\mathbf{v}}$ is known. The parameters $\hat{a}$ and $\hat{b}$ that minimizes the sum of the squared error between the linear model and the estimates, i.e minimizes $\sum_m (\hat{v}[m] - \hat{a} \cdot m - \hat{b})^2$, is given as the well-known least-squares solution

$$\begin{bmatrix} \hat{a} \\ \hat{b} \end{bmatrix} = \left[\mathbf{A}^T \mathbf{A}\right]^{-1} \mathbf{A}^T \hat{\mathbf{v}} \tag{2.21}$$

The idea of using least-squares ultrasound strain estimation is not new, and has been covered in (Kallel and Ophir, 1997).

2.5 Elastographic processing

The strain estimators presented earlier calculate the average strain experienced over the small time-period it takes to gather the number of RF frames needed in velocity estimation. Showing these *frame-to-frame* strain values in real time can be problematic if the strain is generated by a periodic force, such as arterial pulsation, because the strain values will themselves be periodic. In a color-coded image this means that to the operator, regions with

constant stiffness will show a sinusoidal change in color with time. Since we ultimately want to quantify relative stiffness of regions, it would be more natural to have an image where regions of equal stiffness are shown with a fixed color over time. In an attempt to achieve this, an elastographic post processing algorithm has been developed.

This elastographic processing is a three step procedure, using the raw strain data as input. The steps are

1. **Finding strain magnitude.** By taking the absolute value of strain, the strain signal gets a DC component which we assume is related to tissue stiffness.

2. **Low pass filtering (in slow time direction).** This extracts the slowly varying and DC component of the strain magnitude signal, resulting in a signal that is fairly stable over time.

3. **Adaptive normalization.** It is the relative difference in strain magnitudes in an image that we are interested in. By normalizing each frame according to the statistical properties of the same frame, a measure of relative stiffness is achieved.

Adaptive Normalization

An adaptive normalization method was also used in the preliminary project, though there were some problems with the method. The old method was based on the mean value μ and the standard deviation σ of the all the pixels in the input frame, where the input frame was the strain magnitude matrix. For an input frame $\hat{\varepsilon}[m,n]$, values which were above or below the three-sigma bounds $\mu \pm 3\sigma$, were thresholded to $\mu \pm 3\sigma$ respectively. Then the thresholded image was shifted and linearly stretched so that the values of the normalized frame $\hat{E}[m,n]$ covered a range of 0 to 1 inclusive, by:

$$\hat{E}[m,n] = \frac{\hat{\varepsilon}[m,n] - (\mu - 3\sigma)}{6\sigma} \tag{2.22}$$

As mentioned there was problems with the thresholding, shifting and scaling done in Eq. (2.23). Images containing noisy regions would cause the standard deviation σ to become large, resulting in an image in where the dynamic range was decided by the noise and not the fundamental, underlying strain signal. Similarly an image which consists only of noise would be scaled to cover the entire colormap, from soft to stiff, which is not acceptable in a clinical setting.

We propose to take advantage of the correlation coefficients when calculating the image statistics. By not including estimates with a correlation coefficient below a certain threshold in these calculations, the effects of noisy estimates can be excluded. Also instead of stretching the values to cover the entire colormap, we instead suggest to just scale, without shifting and thresholding, the image by an adaptive factor as:

$$\hat{E}[m,n] = \frac{\hat{\varepsilon}[m,n]}{\beta\left(\hat{\varepsilon}, C\right)} \tag{2.23}$$

where β is a coefficient that is calculated from the entire input frame $\hat{\varepsilon}$ and the corresponding correlation coefficient frame C.

β is calculated as a two step process. First the strain magnitude values $\hat{\varepsilon}[m,n]$ that have a correlation coefficient $C[m,n]$ below a set threshold, are fixed to zero. Then β is chosen as the value which bounds a user-specified percentage of the values in the image. We have found, through trial-and-error, that a value of 98 % seems to give good results. This means that β is chosen to be the value which 98 % of the pixel values are below, and the remaining 2 % are above. This leads to an image which shows relative stiffness, where a value close to/or above 1 represents soft areas, while stiffer areas will have a value closer to zero.

One has to be careful when scaling an image like this, because it be can difficult to determine if values are realistic or not, since they are adaptively scaled. Further more the input frame is the low-pass filtered *absolute* value of strain, which can enhance noise if the signal is fluctuating around zero. Nevertheless this method is shown to give good results if the fundamental strain signal is periodic and is not so noisy that it fluctuates around zero.

2.6 Median filtering

The median filter is an *order-statistics* filter, widely used to in the field of digital image processing. The median filter replaces a pixel value with the median of the pixel values in an m by n neighborhood of the pixel. This technique can be powerful when it comes to removing noisy outliers, without over-smoothing or corrupting the original image. The median filter has been found to outperform simpler averaging filters for images which has been corrupted by impulse-like noise (Gonzales and Woods, 2008). We use the median filter as a simple post-processing technique to improve the visual appearance of the strain and elastographic images.

CHAPTER 3

Implementation

A major challenge in the preliminary project was the time-consuming testing of different algorithms and their parameters. The typical workflow was to load RF data, do all the signal processing on each frame and subsequently stitch the resulting images into a video/cineloop. If a single parameter changed, this entire process would have to be repeated to observe the effect, which was cumbersome.

To solve this problem a MATLAB framework, complete with a graphical user interface (GUI), was developed. The GUI allows the user to specify any algorithmic parameter, and choose which estimators to use, from a control panel and directly observe the results at any step of the signal chain. As an example, this allows the user to see, in real-time, how changing a velocity estimation parameter will affect the velocity, strain and elastographic images. This not only makes it faster to optimize parameters, but also makes it easier the understand different steps in the signal chain. The GUI also allows the user to scroll between frames, so that values at different points in the time can be evaluated easily. This is important because there can be a big difference in the strain signal at different points in the cardiac cycle.

When loading RF data the program will read acquisition parameters as well, so that the aspect ratio and axis labeling is handled automatically. The framework was designed to be modularized, so that any part of the signal chain can be interchanged if a new estimator is to be implemented. This makes it easy to test new algorithms as well. The MATLAB framework and GUI can be freely obtained from the author by request.

3.1 The graphical user interface

A screenshot of the MATLAB GUI is shown to the right. While it may not be a feast for the eyes, the GUI is an invaluable tool in parameter optimization once it is known what the different switches and inputs control:

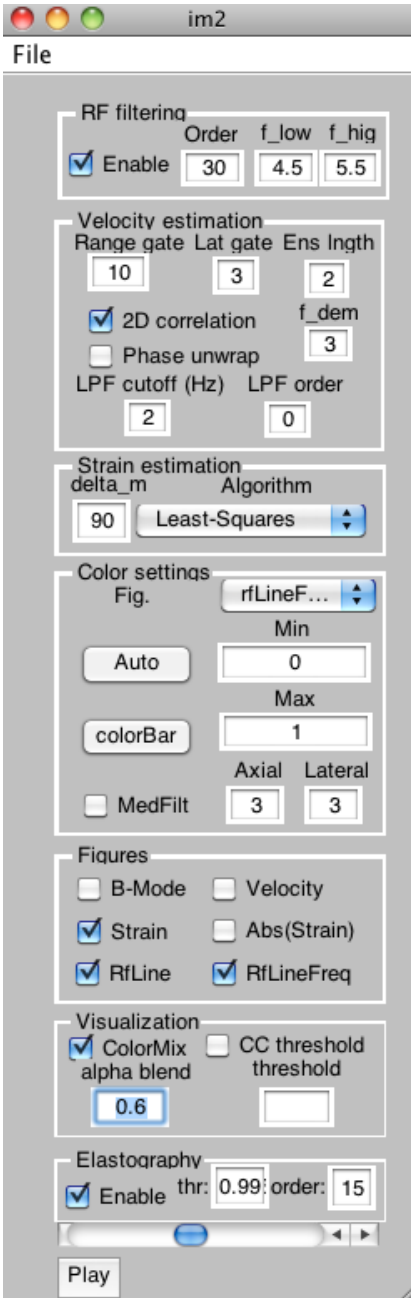

RF filtering
These settings control the bandpass filter that filters each RF scan line in the axial direction. "f_low" and "f_high", given in MHz, are the lower and upper cut-off frequencies for the bandpass filter, while "order" is the filter order. The filter is generated by the *fir1(..)* function.

Velocity estimation
The "Range", "Lat." and "Ens." gate settings control the autocorrelation parameters explained earlier in section 2.1. "2D correlation" enables the 2D-AC estimator, if disabled the 1D-AC estimator is used instead. The "f_dem" parameter is only used for 1D-AC estimation, and controls the demodulation frequency f_0 in Eq. (2.7). The "Phase unwrap" option enables axial phase unwrapping along the scan lines (using the *unwrap(..)* function), which can undo the effect of aliasing in certain cases. The cut-off and order inputs control the optional slow-time filtering of the velocity estimates.

Strain estimation
Controls the length of the axial strain segments by setting the parameter Δm used by the strain estimators. The drop-down menu allows the user choose between least-squares and the central-difference estimation.

Color settings
This panel controls how the images are presented. The range of the colormap can be inputted manually, using the "Min" and "Max" boxes, or the user can let the program automatically pick the range by pressing the "Auto" button. The "colorBar" button produces a color bar which visually shows the mapping between colors and values. The user can also enable median filtering, and change the median filter parameters in the "Axial" and "Lateral" input boxes.

Figures
These checkboxes decide which images are displayed at any given time. In addition to the output from the algorithmic steps, the raw RF signal from a single scan line can be viewed ("RfLine"), or the PSD of the same line ("RfLineFreq"). The PSD figure can be useful to have enabled when tuning the RF filter.

Visualization
Allows the user to alpha blend the output image with the B-mode image in the background, with a user supplied alpha value. The CC threshold option enables correlation coefficient thresholding, with the given threshold.

Elastography
Enables/disables the elastographic processing. The "order" parameter sets the order of the LPF used on the strain magnitude frames. The "thr" parameter is the correlation threshold used in the adaptive scaling in Eq. (2.23).

Slider and playback
By moving the slider at the bottom of the GUI with the mouse, the user can navigate back and forth through the data set. Dragging the slider to the right will advance to the next frame, and to the left to the previous frame. All open figures are updated as soon as calculations have finished. The PLAY button plays through the entire data set.

Example of usage

A screenshot from the program is shown in Fig. 3.1, on page 27, where the outputs enabled are the strain image, the elastographic image, and the RF line in time and in frequency. This allows the user to compare the difference between strain and elastographic processing, while simultaneously inspecting the raw RF signal. If the slider is moved to the next frame, the four figures will update their result accordingly. In this example alpha blending has been enabled, with an alpha value of 0.6. This means that the elastographic and strain images are semi-opaque, so that parts of the B-mode image is blended in the data. The data set used in this screenshot was recorded at the Sintef lab, using an elasticity phantom.

3.2 The ultrasound scanners used

The clinical data available has been acquired using two different systems. Retrospective recordings from the time period 2004–2008 were available, and these recordings were made with a System FiVe (GE Vingmed Ultrasound, Norway) scanner.

The primary system, used for development and testing, was a 2011 SonixMDP scanner (Ultrasonix, Canada). At the time of writing *one* intraoperative, clinical recording has been made with this system, this was recorded in April 2011.

The MDP system has the capability to operate in "research mode," an option which gives the user great freedom to alter parameters involved in the entire ultrasound signal chain. Given this opportunity, we wanted to see if results could be improved by changing the transmitted pulse. In order to find a suitable transmit pulse for strain estimation, we must first understand what kind of pulses the SonixMDP system is capable of transmitting.

The SonixMDP pulser

An ultrasound system has a circuit responsible for generating the electronic pulse which the ultrasound transducer converts to pressure waves. This circuit is known as a pulser, and the pulser in the MDP scanner is a *tri-level pulser*, i.e it can generate three possible voltages; Either a fixed positive, zero, or a fixed negative voltage. The MDP pulser is a discrete circuit, clocked with a frequency of 40 MHz. Consequently the pulser output can only change at fixed points in time, with a resolution of $1/(40\,\mathrm{MHz}) = 25\,\mathrm{ns}$. If we require a pulse to consist of at least one positive and one negative

part, the lowest fundamental period possible is 50 ns. For such a pulse, the fundamental transmit frequencies f_{tx} achievable is governed by the relation

$$f_{tx} = \frac{40}{n} \text{ MHz}, \quad n = 2, 4, 6 \ldots \tag{3.1}$$

A pulse may be described by the transmit frequency and a specified amplitude pattern. To describe a tri-level pulse, the same convention as the MDP system is adopted: The symbols {+, 0, –}, corresponds to a positive/zero/negative amplitude lasting a half period of the fundamental period. As an example, a pulse with $f_{tx} = 5\,\text{MHz}$ and waveform "+ – +" is shown in Fig. 3.2. Note that pulses are not uniquely described by f_{tx} and the waveform; As an example the pulse $p_1 = \{+-, f_{tx} = 5\,\text{MHz}\}$ and the pulse $p_2 = \{++--, f_{tx} = 10\,\text{MHz}\}$ are identical. By not allowing the repetition of the same symbol twice, this ambiguity is removed. This means that only alternating pulses, in the form of $\{+-+\ldots\}$ are allowed. In this way the parameters that define a pulse can be restricted to the number of half periods (N_{hp}) and the transmit frequency f_{tx}.

Choosing the transmitted pulse

To look into the effects of changing the pulse form and frequency, a high attenuation phantom was used. The phantom had an attenuation coefficient of 0.7 dB/(MHz cm), which is similar to that of the brain (Cobbold, 2007). The probe used was the "L14-5/38" supplied by Ultrasonix, which is a linear probe usable from 5 to 14 MHz according to the manufacturer. The RF sampling frequency was 40 MHz.

During initial experimenting with pulses, we noticed little visible change in the image with increased transmit frequency. This was unexpected, as an increase in transmit frequency should give increased axial resolution and decreased penetration. To investigate this phenomenon, the power spectral density (PSD) of the received RF signal was studied for four different pulse lengths, transmitted at both 5 and 10 MHz. The PSD was estimated using Welch method on each scan line, and then averaging the resulting PSDs from each scan line. The imaging depth was set to around 2.5 cm.

The plot in Fig. 3.3 shows the theoretical power spectrum of the 5 MHz pulses together with the estimated power spectrum of the echo signal. The spectrum from the 5 MHz pulses show a main lobe centered around 5 MHz, as expected. It is seen that the width of the main lobe decreases for every increase in the number of half-periods N_{hp}. This is well known from Fourier theory; a longer pulse in the time domain gives a more narrow banded pulse in the frequency domain.

The same plot, but for 10 MHz pulses, is shown in Fig. 3.4. The received spectrum from these pulses have a main lobe located somewhere in the 4–6 MHz range. This came as a surprise since we had expected a main lobe centered around 10 MHz. This explains why there was little difference in the image when switching between 5 and 10 MHz, since in both cases most of the signal energy is around 5 MHz anyway.

However when comparing the received spectrum to the theoretical spectrum, a possible explanation for the apparent lack of energy at 10 MHz can be found. Notice that since the temporal length of the 10 MHz pulses are half the length of the corresponding 5 MHz pulse, the width of the main lobe increases accordingly. If, for simplicity, we assume that the entire received signal is from exactly 2.5 cm depth, the attenuation is $0.7\,\mathrm{dB/(MHz\,cm)} \cdot 4\,\mathrm{MHz} \cdot 5\,\mathrm{cm} = 14\,\mathrm{dB}$ at 4 MHz, and correspondingly 35 dB at 10 MHz. This is a difference in attenuation of 21 dB.

Looking at the *theoretical* spectrum for the 10 MHz, five half-period pulse, shown in black, the side lobe centered at 4 MHz is approximately 10 dB lower than the main lobe at 10 MHz. The *received* signal now shows that the 10 MHz lobe is around 10 dB *lower* than the 4 MHz lobe. This means that the main lobe has been attenuated around 20 dB more than the side lobe, which is close to what our simplified calculations predicted. In addition to frequency-dependent attenuation, the probe itself has a frequency response, which judging by the received signal is probably more favorable for pulses in the 5 MHz range.

Thus there seems be be three reasons as to why imaging at 10 MHz is difficult with the MDP system: Significant side lobes are generated by short pulses at 10 MHz, the high frequency-dependent attenuation of brain tissue, and the frequency response of the probe. Due to these factors, it was decided to use 5 MHz pulses for imaging.

By inspecting the B-mode image the number of half-periods was set to 3. If the number of half-periods was increased above this, a noticeable degradation in axial resolution was seen. A shorter pulse gave penetration problems, with little signal seen in the depth of the phantom.

It is not known what kind of pulse form was used for the GE system, only that the center frequency was 8 MHz.

3.3 The elasticity phantom

A data set from an elasticity phantom has been used to test the algorithms, filters and features implemented. This data set is the same that was used in the Master's project. Using an elasticity phantom, we know the stiffness

distribution a priori, so it is easier to judge if the results seen are correct or not.

The elasticity phantom is made of a uniform material, but has three stiff inclusions with higher Young's modulus than the "background" material. The echogenicity of the background and the inclusions is the same, so the inclusions will not be visible in the B-mode image. The imaging probe is fixed to a motor which pushes the probe down on the phantom, compressing it with a sinusoidal force. Due to the time-varying compression the phantom material will move with respect to the probe, leading to a measurable, time-varying velocity distribution in the phantom.

The B-mode and strain image of the phantom, from a single frame, is shown in Fig. 3.5 on page 31, with the inclusions clearly visible in the strain image, while they are not visible in the B-mode image. Since the velocity estimation results were covered in detail in (Boerstad, 2010), they will not be covered again in this thesis. Specifically the phantom data will be used to show the effects of all methods that were not a part of project, namely least-squares strain estimation, the updated elastographic processing, correlation coefficient thresholding and median filtering.

3.4 Arterial pulsation

The key assumption behind our strain imaging setup, is that the deformation caused by pulsation of the cerebral arteries is strong enough to be detected by ultrasound, and is sufficient to generate measurable tissue deformation. From the intraoperative B-mode cineloops, **no visible motion is seen**. The hypothesis it that there is still some movement present in the RF signals, and that this movement can be estimated. Nevertheless due to the lack of visible movement, we know that the motion generated, if any, is very small.

The lack of visible motion makes it difficult to judge if estimated velocity values are real, or if they are simply caused by noise. Lacking a model of the pulsation of the cerebral arteries, we are also uncertain of what pattern to look for. We assume that the measured velocity will at least be periodic, with a period following the pulse of the patient.

To attempt to quantify the *shape* of the velocity curve, we have looked at the arterial pulsation in a more accessible part of the body, namely the carotid artery. The carotid artery supplies the head with blood, and there is one on each side of the neck. While the dilation of the cerebral arteries will be different from that of the carotid artery, we hope that this can give us a rough idea of the shape we look for.

An ultrasound recording of the left carotid artery was made, over several heart cycles. The probe was aligned along a sagittal plane, and was attempted positioned so that the axial direction was perpendicular to the carotid artery wall. In other words the probe was placed so that the movement was purely axial. A single b-mode frame from the recording is shown in Fig. 3.6, on page 32, with the carotid artery wall outlined in red. The pulsation of carotid artery is large and is easily seen in the B-mode cineloop.

Since the movement is visible on the B-mode image, the wall displacement can easily be tracked with time. To crudely estimate the displacement, a single point on the anterior carotid wall was tracked, with a simple neighborhood search for each frame. Once the displacement is known, we can differentiate with respect to time to find the velocity.

The tracked wall displacement, over a period covering roughly four cardiac cycles, is shown as the top curve in Fig. 3.7. The wall displacement is clearly of a periodic nature, as expected. Some high-frequency noise is seen in the displacement curve, which could be a result of poor tracking or shaking of the operator holding the probe. Nevertheless, a clear, pulsatile pattern is seen. The carotid artery diameter and pressure relationship has been found to be linear (Sugawara et al., 2000), so we assume that the displacement curve is roughly proportional to the pressure within the carotid artery.

The numerical derivative of the displacement curve is shown in the lower plot in Fig. 3.7. This curve is quite noisy, but there is a clear spike pattern, most likely caused by the systole. It is difficult to say how relevant the velocity curve from the carotid artery is to velocity curves from the brain, but at the very least we would expect to see some sort of spike pattern in the cerebral arteries as well.

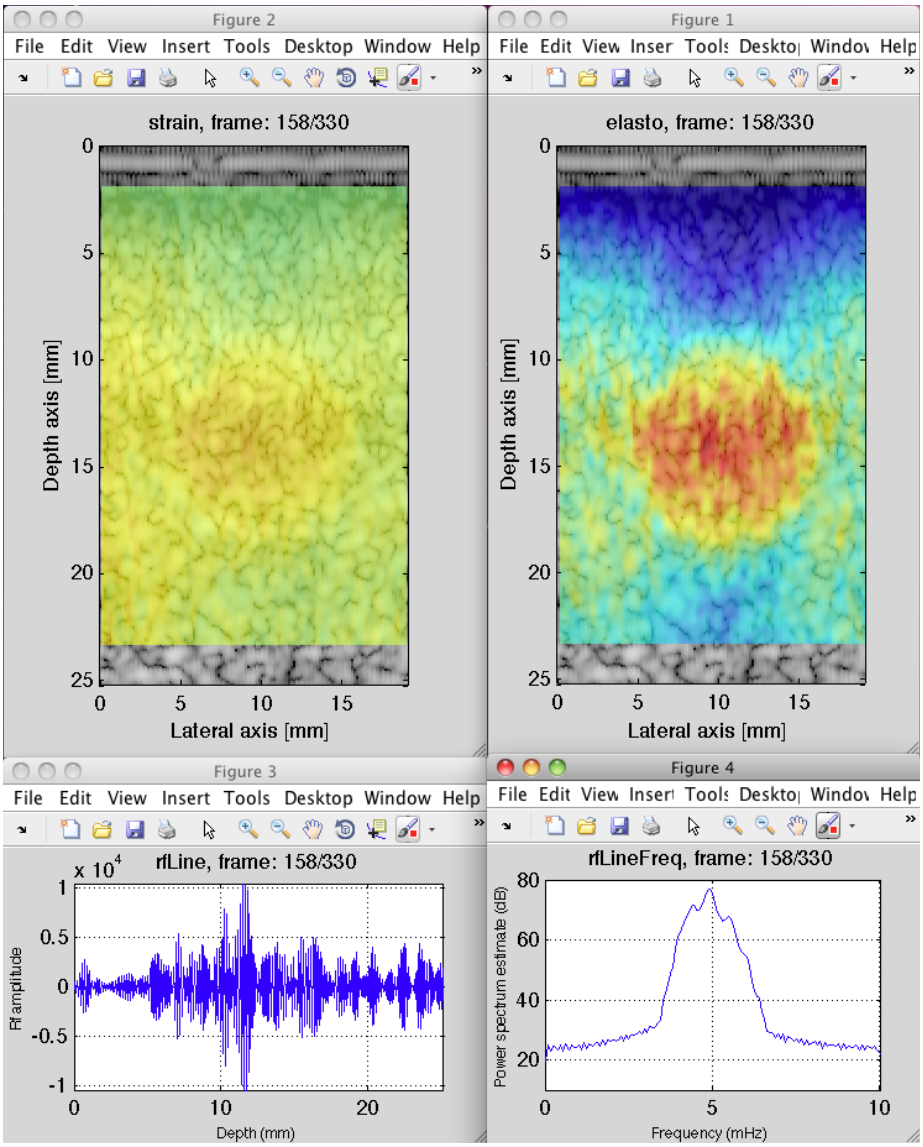

Figure 3.1: Sample screenshot from the MATLAB program. Top left shows the strain window, top right shows the elastographic window, bottom left shows one of the RF lines in the time domain, and bottom right shows the same RF line in frequency domain.

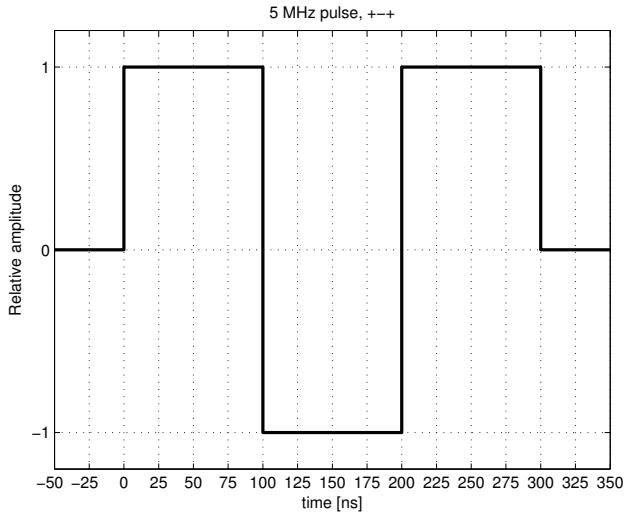

Figure 3.2: The pulse $\{+-+, f_{tx} = 5\,\mathrm{MHz}\}$ illustrated in the time-domain

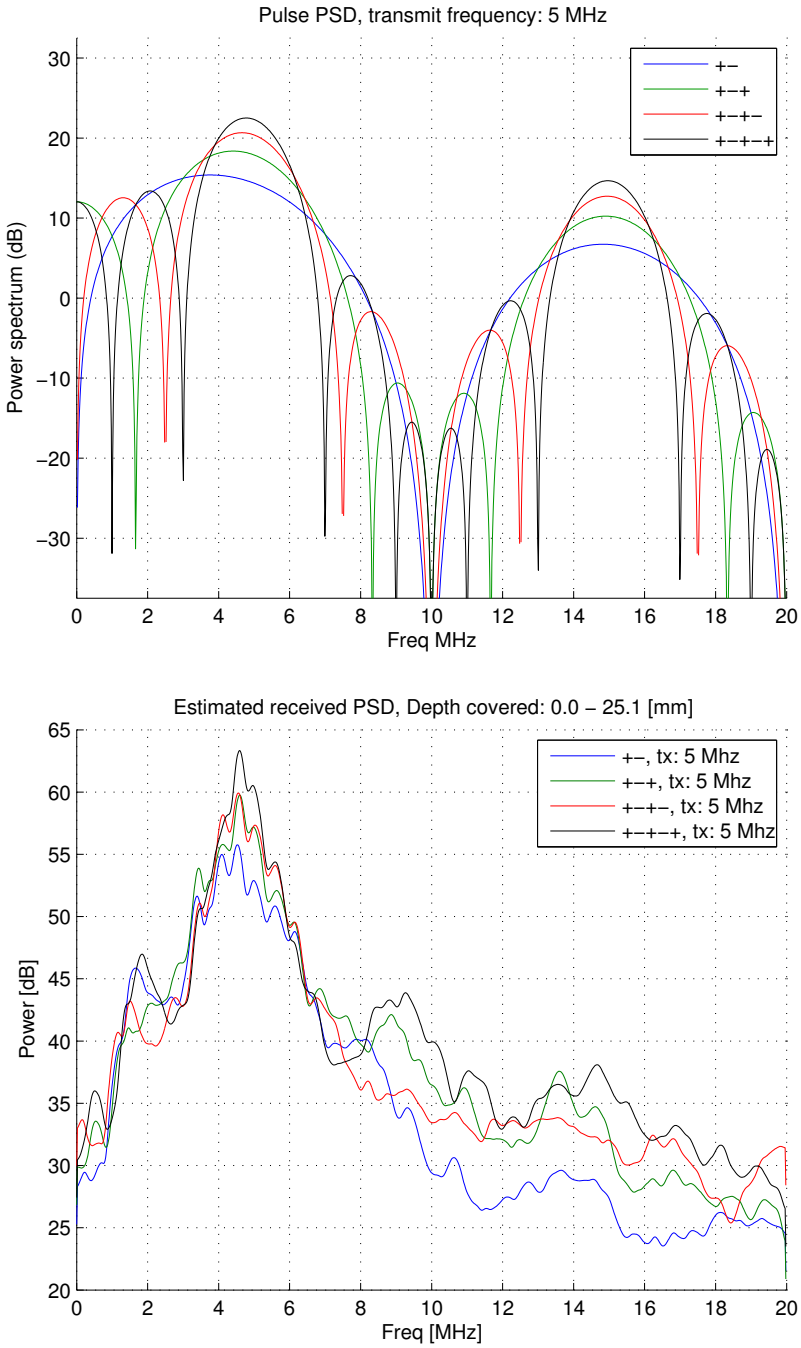

Figure 3.3: The top plot shows the PSD for 5 MHz pulses with 2, 3, 4 and 5 half periods. The bottom plot shows the estimated PSD of the *received* echo-signal when transmitting these pulses.

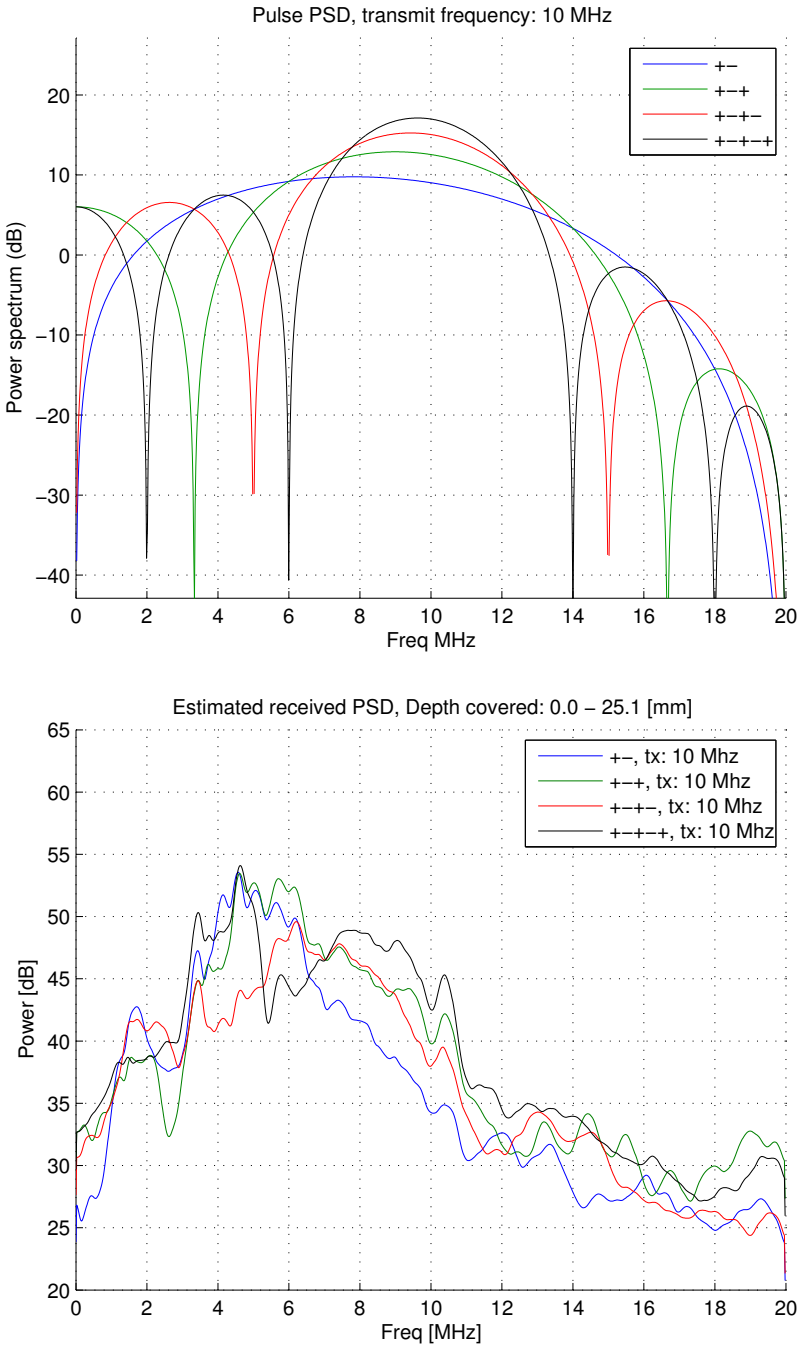

Figure 3.4: The top plot shows the PSD for 10 MHz pulses with 2, 3, 4 and 5 half periods. The bottom plot shows the estimated PSD of the *received* echo-signal when transmitting these pulses.

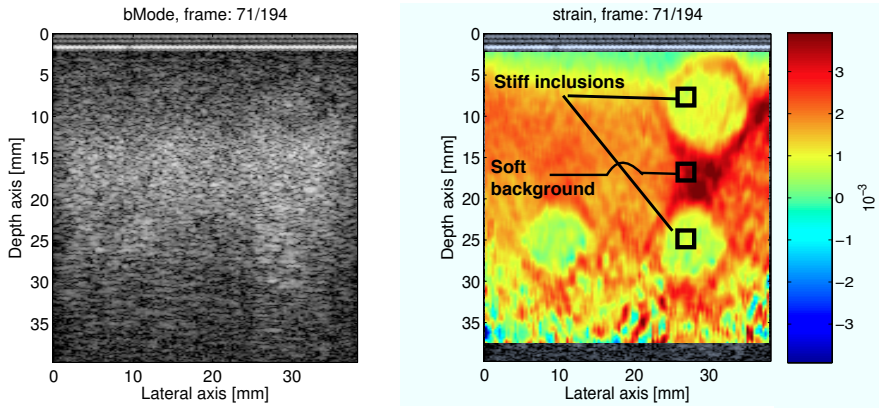

(a) B-mode image (b) Strain image

Figure 3.5: The B-mode and strain image from a single frame of the phantom data

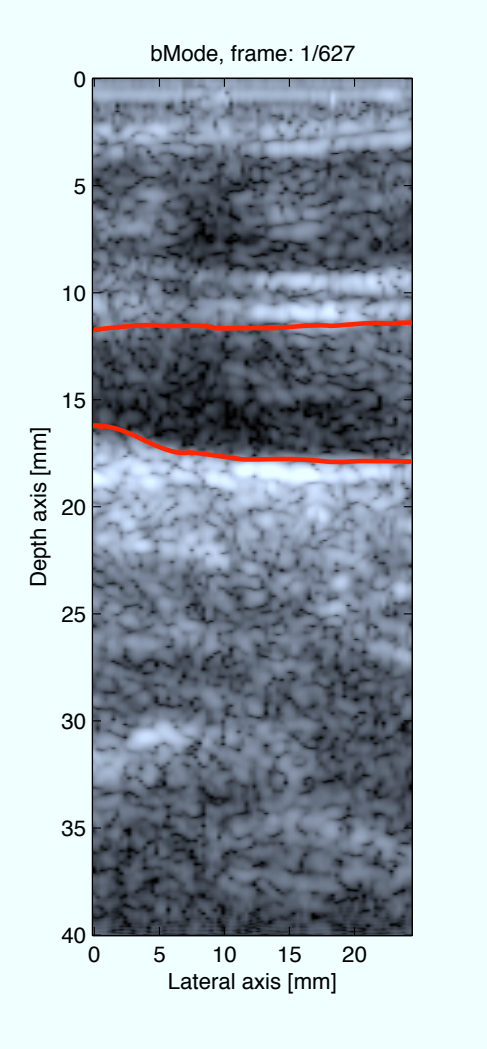

Figure 3.6: The carotid artery walls outlined in red (top = anterior wall, bottom=posterior wall).

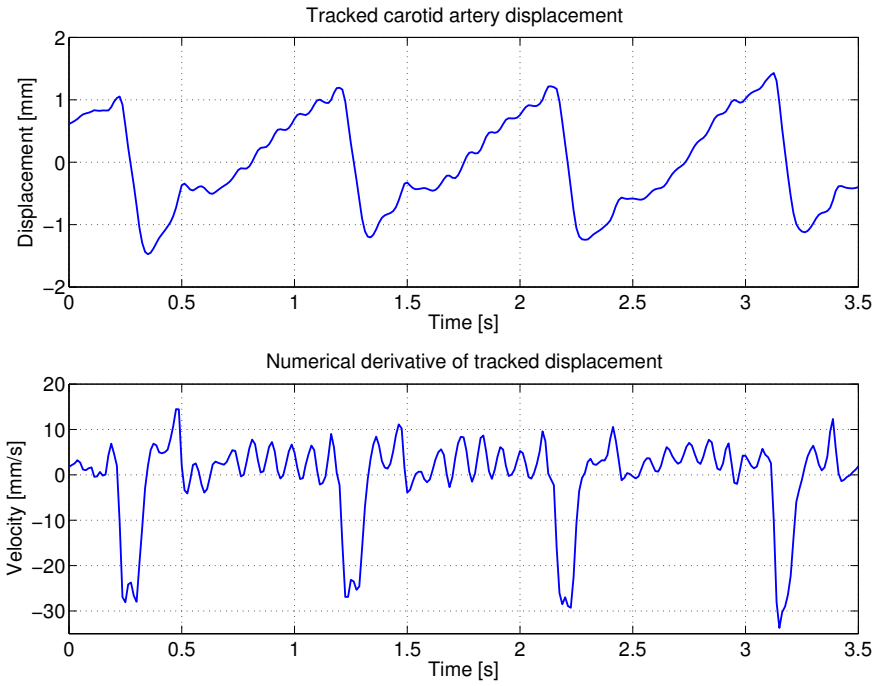

Figure 3.7: Tracked displacement of the carotid artery (top curve) and corresponding velocity found by numerical differentiation (bottom curve)

CHAPTER 4

Results

This chapter is divided into two parts. The first part presents the results from the algorithms, based on the elasticity phantom. Then our findings from intraoperative, clinical data sets is presented. The acquisition parameters for the phantom and clinical recordings in shown in Table. C.1, in appendix C on page 73. Appendix C also contains the algorithmic parameters used to generate all the figures in this chapter.

4.1 Central-difference vs least-squares strain estimation

A comparison between the central-difference (CD) and the least-squares (LSQ) strain estimators is shown in Fig. 4.1. The estimators are compared with two different velocity inputs. The first input, shown in the top row, was produced with using a long range gate ($\mathbf{M} = 60$), which smoothes the velocity estimates in the axial direction. The difference between the estimators on this input is not very noticeable.

The second input, shown in the bottom row, was produced with a shorter range gate ($\mathbf{M} = 6$), which means that the velocity estimates are noisy in the axial direction. The difference between the estimators is easily noticeable, with the CD values being more noisy than the LSQ values.

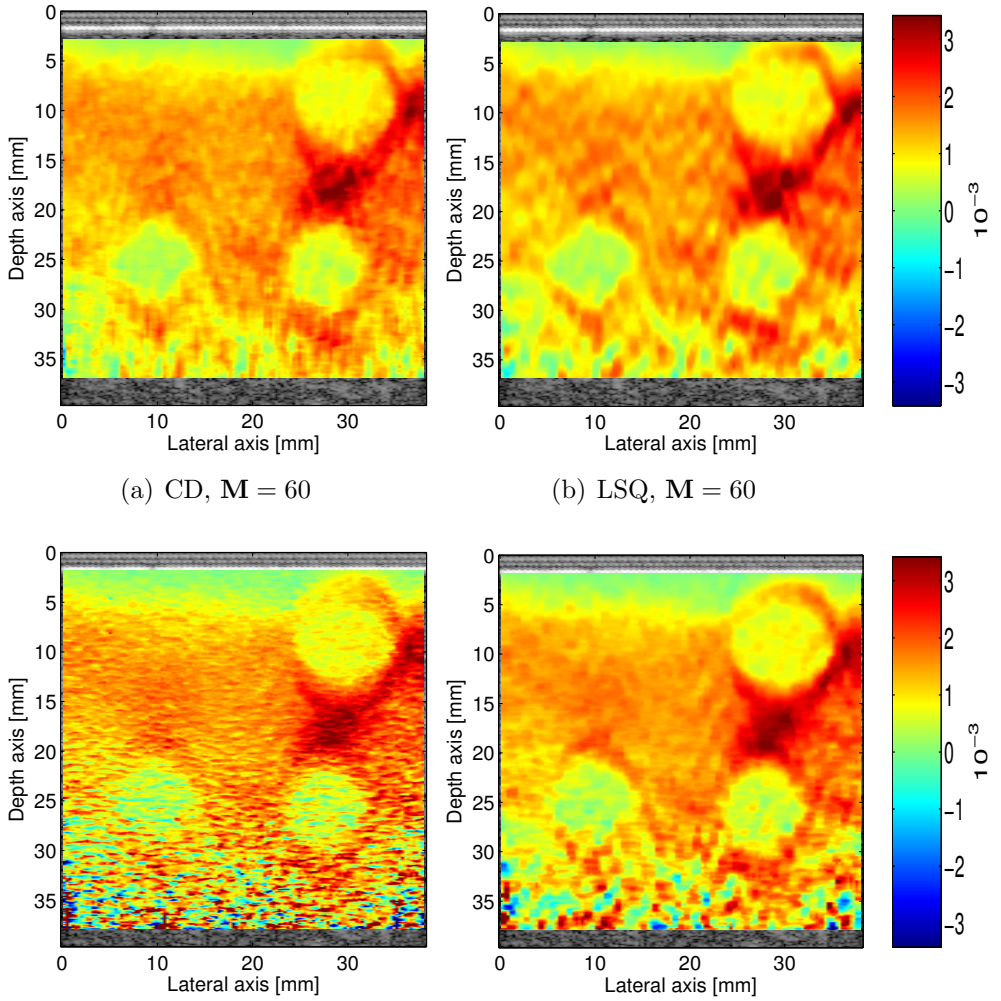

(a) CD, $\mathbf{M} = 60$ (b) LSQ, $\mathbf{M} = 60$

(c) CD, $\mathbf{M} = 6$ (d) LSQ, $\mathbf{M} = 6$

Figure 4.1: The output of CD (left column) and LSQ (right column) strain estimation for two different input, where the difference between the input is the range gate $\mathbf{M}$. The length of an axial segment (Δm) is 90 samples for all images

4.2 Elastographic processing

In order to illustrate the effect of elastographic processing, it is necessary to look at both the strain and elastographic values over time. Strain values, from two of the inclusions and from the background material, is shown in Fig. 4.2. It is seen that the shape of the strain curve does not change

much in the three different regions, but the amplitude varies with regions stiffness. As discussed in section 2.5, these strain images do not look good when displayed in a cineloop, because of the large variation in strain with time.

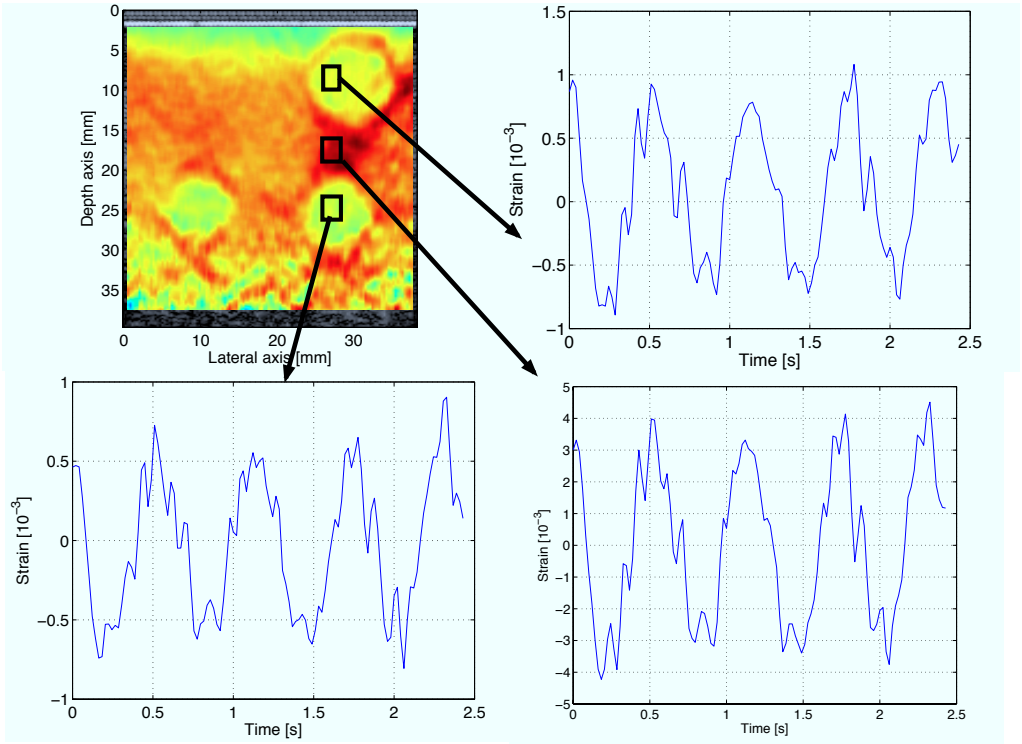

Figure 4.2: Strain image from the phantom in the top left, with extracted strain values over time from the three regions marked in the image

The elastographic processing is used to solve this problem, and the output of the three intermediate steps, that is strain magnitude, low pass filtering and adaptive scaling, is shown in Fig. 4.3. It is seen that the relative stiffness signal is much smoother than the raw strain signal.

The elastographic image and curves corresponding to the strain image just shown, is illustrated in Fig. 4.4. It is seen that the elastographic curves are much smoother than the strain corresponding strain values. A big difference in relative stiffness between the soft background and the stiffer inclusions is also seen. Note that a lower elastographic value means corresponds to a lower strain magnitude, which in general means a stiffer material.

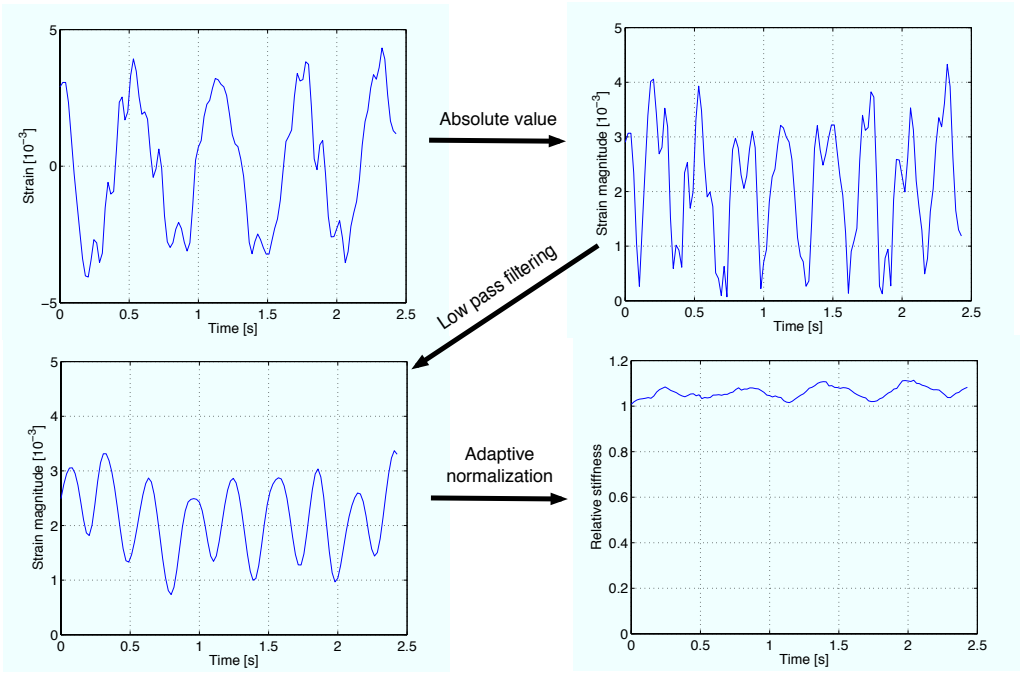

Figure 4.3: The different steps of elastographic processing. Top left: Raw strain. Top Right: Strain magnitude. Bottom left: Low pass filtered strain magnitude. Bottom Right: Final result after adaptive normalization

4.3 Median filtering

To illustrate the effect of the median filter, a strain image with and without 3x3 median filtering enabled is shown in Fig. 4.5. The strain image was made with input data that used a low lateral gate (see appendix for algorithmic values), to deliberately show discontinuities in the lateral direction. It is seen that the median filter removes most of these discontinuities, without any visible degradation of spatial resolution.

4.4 Correlation coefficient thresholding

The correlation coefficients from the phantom data is shown in Fig. 4.6. It is seen that the correlation coefficients decrease with depth in this image.

It was mentioned in section 2.2 that the correlation coefficients could be used to hide noisy estimates from the images, by correlation coefficient

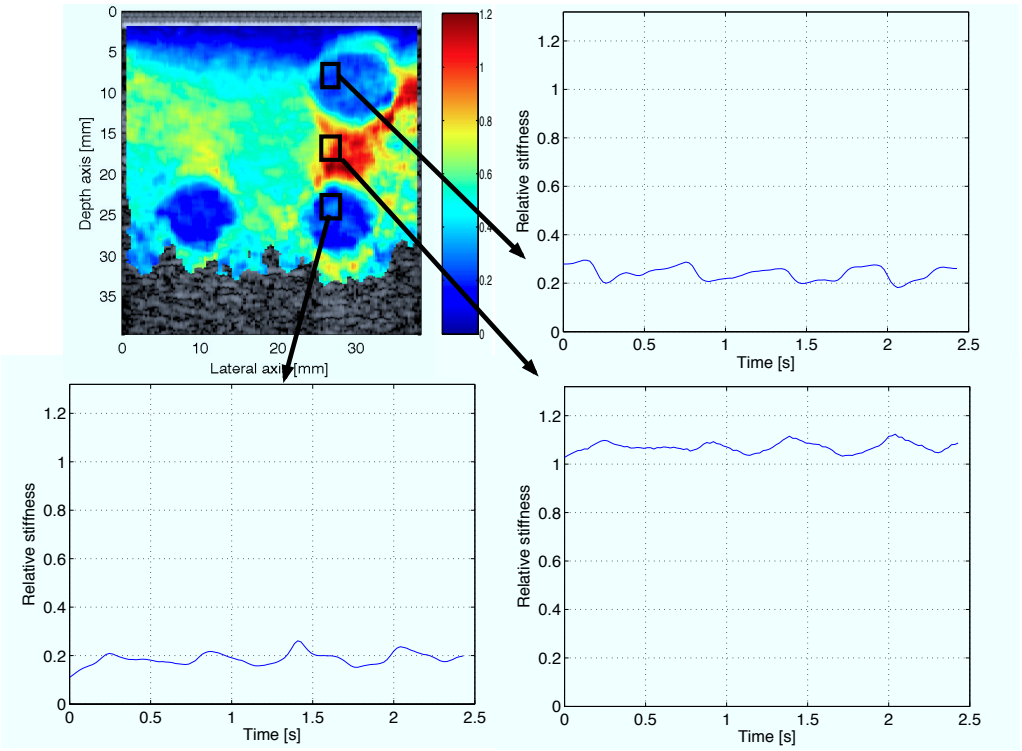

Figure 4.4: Same curves as in Fig. 4.2, shown after elastographic processing

thresholding. The effect of such a thresholding, on the elastographic image, is shown for two different thresholds in Fig. 4.7. It is seen that the more of the noisy estimates at the bottom of the image are removed with an increasing threshold.

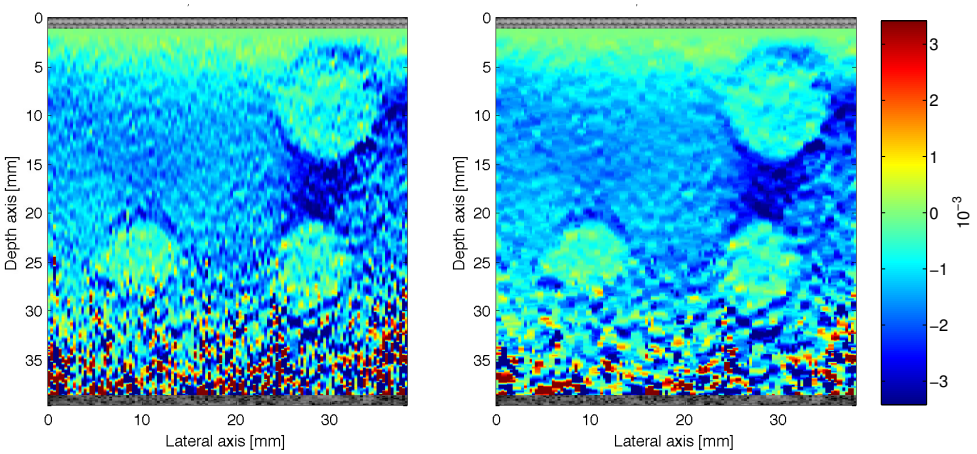

(a) Without median filtering (b) With 3x3 median filter

Figure 4.5: Strain image shown with and without 3x3 median filtering enabled

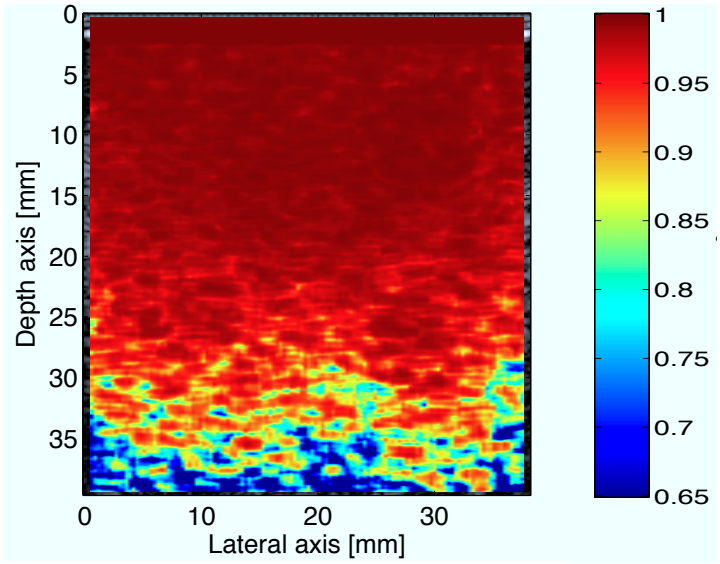

Figure 4.6: The correlation coefficients of the velocity estimates.

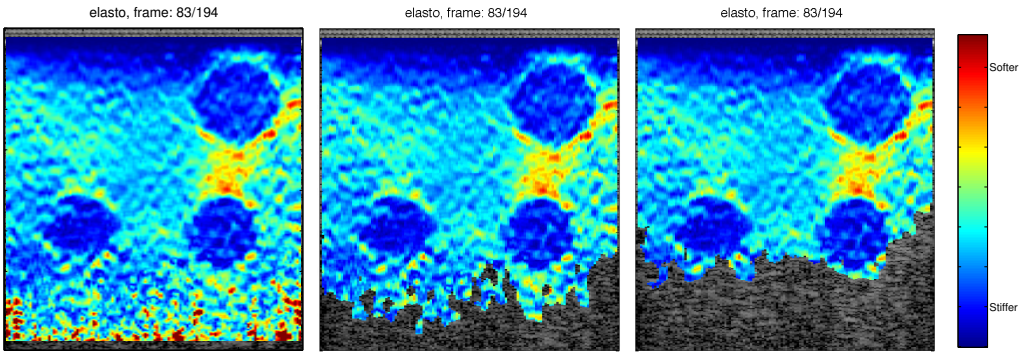

(a) No CC cutoff (b) CC cutoff = 0.75 (c) CC cutoff = 0.85

Figure 4.7: Effect of correlation coefficient thresholding on an elastographic image

4.5 Clinical data set 1 - hippocampal tumor

The patient had a tumor located in the hippocampus, with a long-axis diameter of approximately 15 mm. The screenshot in Fig. 1.3, which was used to illustrate the SonoWand system in Chapter 1, is from the same patient and gives an informative view of the tumor location. It is pointed out that the ultrasound image in the screenshot was recorded with the SonoWand system, which is why the image is not identical to the one presented here, which is from the Ultrasonix system.

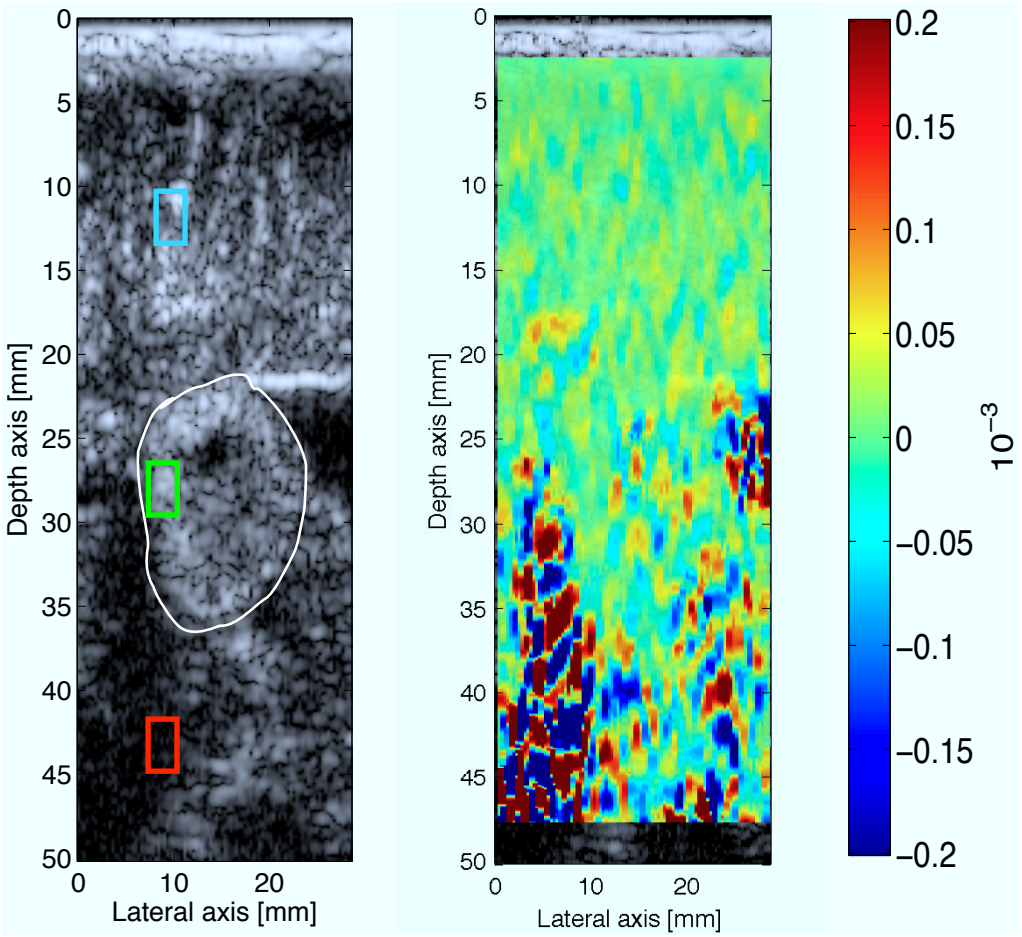

Figure 4.8: B-mode and strain image of a brain tumor in the hippocampus. The cyan rectangle marks a region of healthy tissue, the green rectangle a region of tumorous tissue and the red a region from of a ventricle. The tumor is the oval shaped object enclosed by the white boundary.

The intraoperative B-mode and strain frame from this patient is shown in Fig. 4.8. The region that is believed to be the tumor has been identified manually based on the B-mode image, with our interpretation of the tumor border shown in white. The dark structures in the lower left corner, and on the right hand side at around 25 mm depth, are believed to be fluid-filled ventricles. It is seen that the strain values in these regions fluctuate significantly with small changes in position, and fall outside both the positive and negative range of the color map. The remaining strain values are of low amplitude and do not seem to follow any obvious pattern.

Velocity and strain curves

Three regions of interests (ROIs) have been marked by colored rectangles in Fig. 4.8, and the velocity and strain over time from these regions have been extracted. The first region represents what is believed to be healthy tissue, the second region tumorous tissue and the third region represents an area of high noise (from a ventricle). The spatially averaged velocity and strain curves from these regions are shown in Fig. 4.9.

These curves reveal that the estimates suffers from a low signal-to-noise ratio, and it is difficult to extract any useful information at all from the curves due to noise. To see if there is any periodic components in the curves, which could be caused by arterial pulsation, the estimated PSD of the velocity curve from the tumor region is shown in Fig. 4.10.

The PSD of this velocity curve, shown in blue, reveals two peaks. One at around 1 Hz and another around 10 Hz. To extract the 1 Hz signal component, a low pass filter was used. The filter response and the resulting filtered signal PSD is also shown in Fig. 4.10.

The filtered curves are presented in Fig. 4.11. The velocity curves from the normal and tumorous tissue now appear to have a clear, periodic pattern with a fundamental frequency of 1 Hz. These same curves has shapes that are significantly different than the shape of the curve from the noisy region. The maximum velocity measured is around -0.1 mm/s, disregarding the results from the noisy region.

Looking at the filtered strain curves, to the right in Fig. 4.11, does not provide much information. A periodic pattern is seen in the strain curve from the tumorous tissue, while the curves from the normal tissue and noisy region appear more random. The three strain curves all have different shapes.

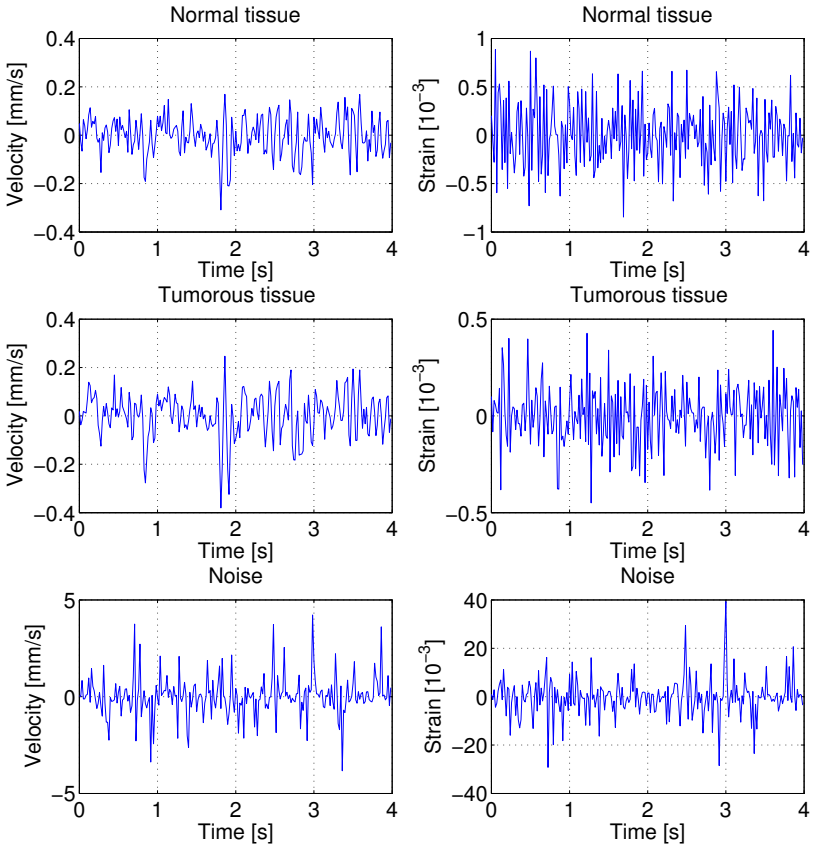

Figure 4.9: Velocity (first column) and strain curves (second column), extracted from the ROIs shown in Fig. 4.8

Elastographic values

The elastographic image and corresponding curves are shown in Fig. 4.12, with correlation coefficient thresholding enabled. It is seen from the elastogram that a large portion of the estimates are removed, meaning that they have a lower correlation coefficient than the visible values. The elastographic image itself reveals no obvious structures, and looks noisy.

Inspecting the elastographic curves shows that the values from the noise region are far above the range of the color map. The remaining curve from the tumorous and healthy tissue show some fluctuation with time, with the tumorous tissue values mostly being higher than the ones from the healthy

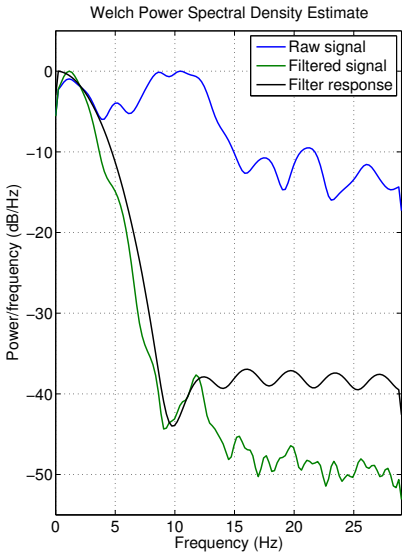

Figure 4.10: Normalized PSD estimates of the tumorous tissue velocity curve, the low pass filter response, and the PSD of the signal after filtration

tissue.

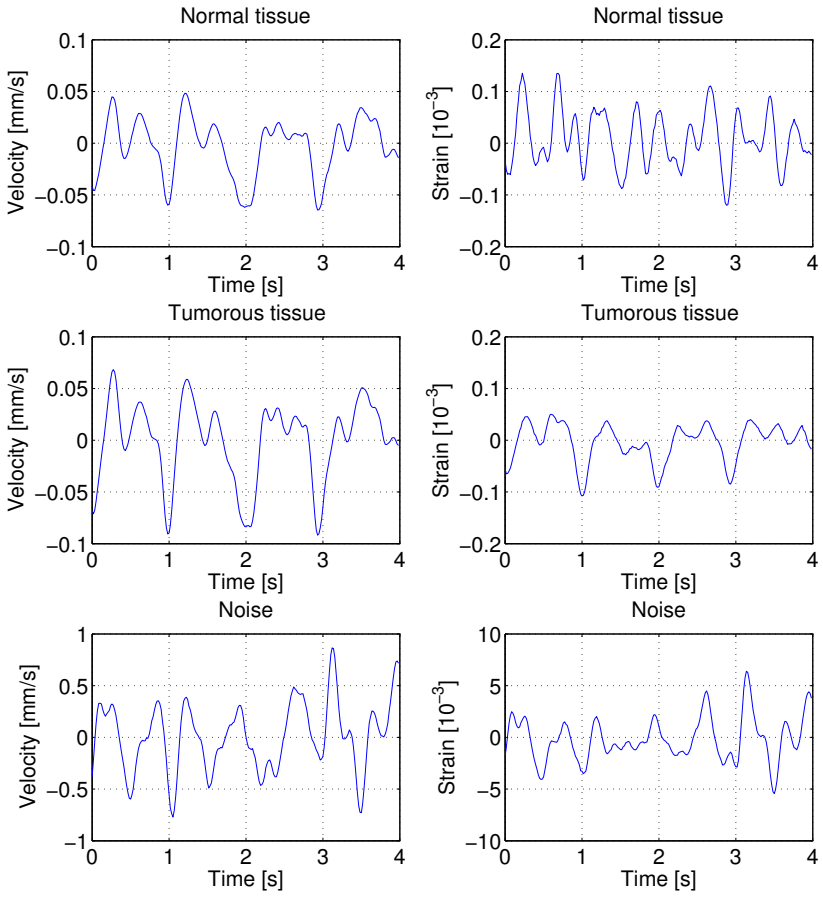

Figure 4.11: The low pass filtered velocity and strain curves, unfiltered curves shown in Fig. 4.9

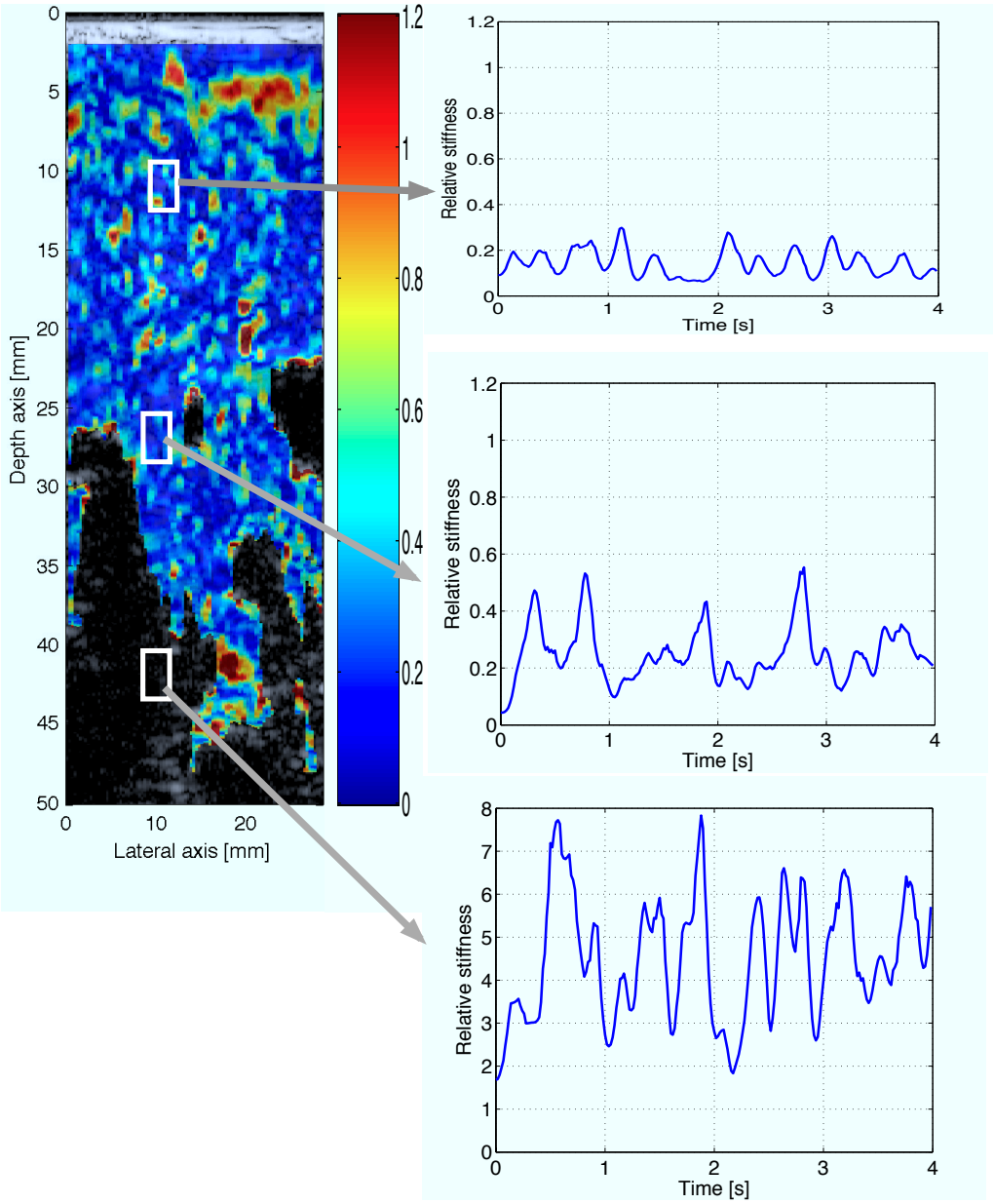

Figure 4.12: The elastogram (top left) shown with correlation coefficient thresholding enabled. Elastographic curves from healthy tissue (top right), tumorous tissue (middle right) and a region of noise (bottom right) is also shown

4.6 Clinical data set 2 - metastasis

The B-mode and strain image from the second data set is shown in Fig. 4.13. The entire tumor border cannot be clearly identified from the B-mode image, but the part of the border which *can* be determined is shown in white. It is unknown if the upper left region of this image is made up of tumorous or healthy tissue. This tumor is a *metastasis*; it has spread to the brain from another part of the body.

The strain image indicates uniform strain values inside the tumor, and a sharp transition of the strain values is present in the upper part of the image. We also see a region in the lower right corner where there is low

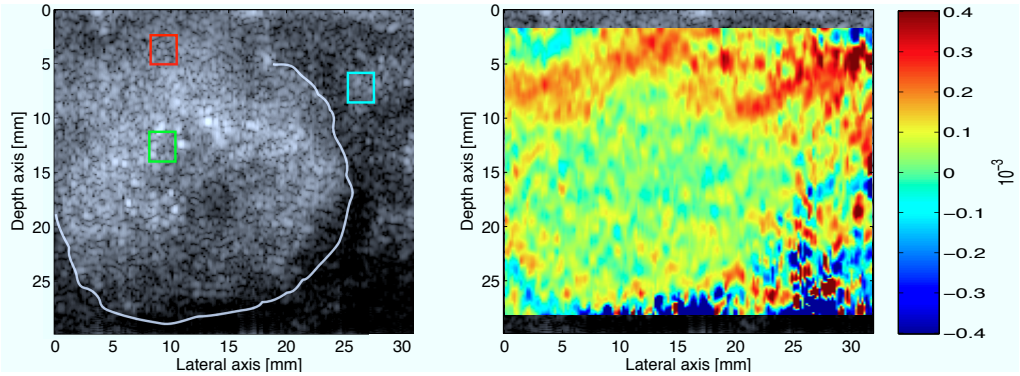

Figure 4.13: Intraoperative B-mode and strain image of the metastasis. The red rectangle marks a region non-classifiable tissue region. The green rectangle represents tumorous tissue, while the cyan rectangle represents healthy tissue. Parts of the tumor border is outlined in white.

signal strength, leading to what appears to be noise in the strain estimates.

Velocity and strain curves

The velocity and strain curves from the ROIs marked in the B-mode image are shown in Fig. 4.14. Though only 1.5 seconds of data is available, a periodic pattern with frequency around 1 Hz looks to be present in the velocity curves. The peak velocity is around -0.4 mm/s. The velocity curves from the three regions all seem to follow the same governing pattern.

A periodic shape, similar to that of the velocity values, is seen in all the strain curves. The peak strain values are around $-0.12\,\%$ for the normal tissue, $-0.08\,\%$ for the unknown tissue, and $-0.04\,\%$ for the tumorous tissue. In general the normal tissue shows the highest strain amplitude, the

unknown tissue slightly lower amplitude, and the tumorous tissue shows the lowest amplitude.

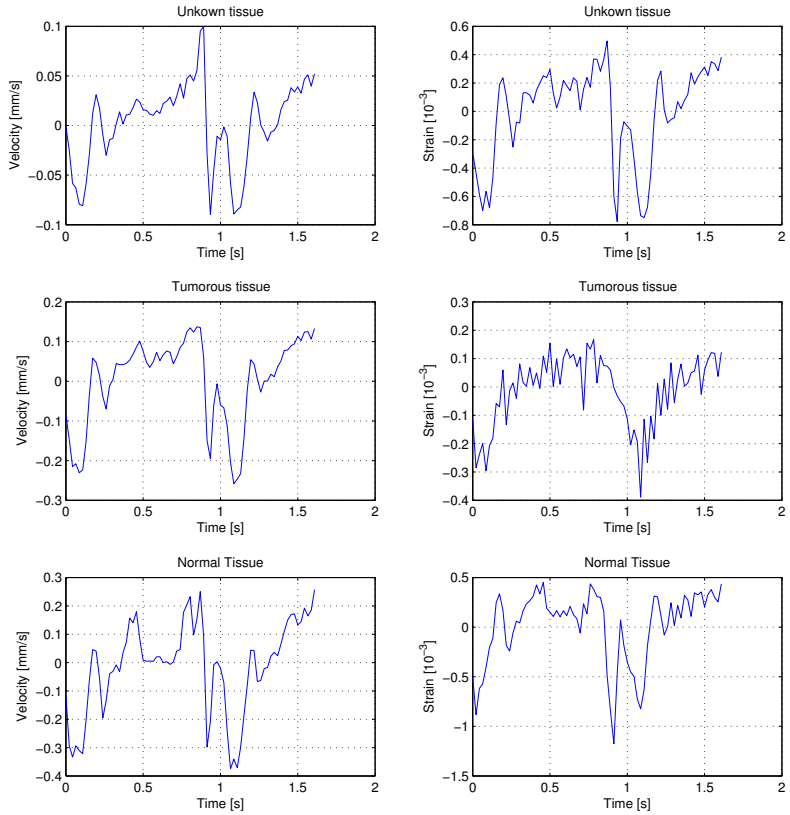

Figure 4.14: Velocity (first column) and strain curves (second column), extracted from the ROIs shown in Fig. 4.13

Elastographic image

The elastographic image, with correlation coefficient thresholding, together with the elastographic curves from the ROIs are shown in Fig. 4.15. It is seen that the estimates in the lower region of the image have been removed, due to low correlation.

The elastographic values in the healthy and the unknown tissue regions fluctuate some over time, while the values from the tumor are fairly stationary. A clear relationship between the elastographic values are seen; The healthy tissue is always has a higher elastographic value than the unknown tissue, which again always has higher values than the tumorous tissue.

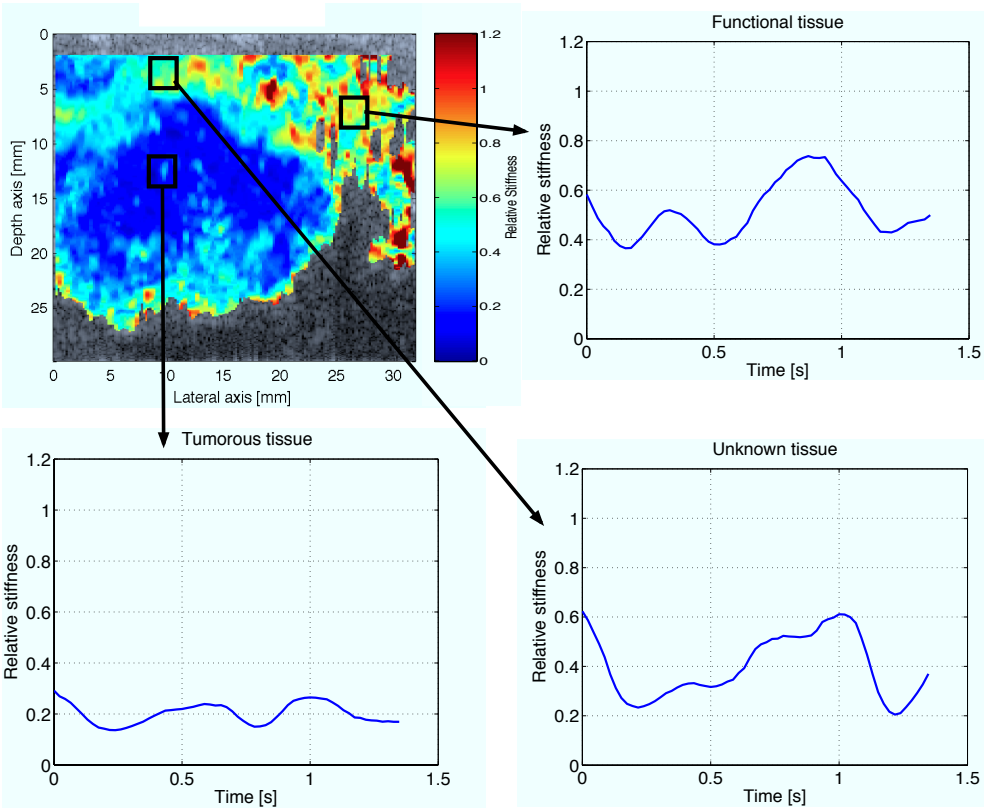

Figure 4.15: Elastogram with correlation coefficient thresholding, together with elastographic values over time.

CHAPTER 5

Discussion

We start with discussing the algorithmic results from all three data sets, and then continue by looking at, and interpreting, the findings from the clinical data sets.

5.1 LSQ estimation

Our experience with the least-squares strain estimator is that it produces images of equal or better quality than the central-difference estimator, depending on the input. If the velocity data are smooth in the axial direction, then the difference between the methods is subtle. This was illustrated in Fig. 4.1 (a) and (b), which used a large range gate in the velocity estimation step, resulting in low-noise velocity estimates at the expense of decreased axial resolution. The figure shows no significant difference between the two estimators.

If the velocity estimates are noisy in the axial direction, then the LSQ estimator gives better results, as seen in Fig. 4.1 (c) and (d). The fact the the difference between the methods increases with noise, can also be seen by looking at the strain estimates at different depths. The difference between the two estimators increases with depth, and we know from the correlation coefficients in Fig. 4.6, that the estimates at the bottom of the phantom are more noisy.

While not shown in the results, we also found that the difference between the estimators is reduced by using a shorter axial length Δm. This is not surprising as the LSQ estimator degenerates to the CD estimator with $\Delta m = 1$. However, decreasing Δm results in more noisy estimates (Boerstad, 2010). For a theoretical discussion of the statistical properites of

strain estimation using least-squares see (Kallel and Ophir, 1997), which predicts that LSQ estimation will give improved SNR compared with CD estimation, which agrees with our findings.

The only advantage we see with using the CD estimator, is that it is slightly faster to compute. However with the implementation given in appendix A, the LSQ estimator implemented in MATLAB, uses less than 0.01 seconds to compute a typical strain image. Thus we see no reason to not use the LSQ estimator.

5.2 Elastographic processing

The degree of success of the elastographic processing has been found to be strongly dependent on the input data. The idea behind the processing, as discussed in the theory chapter, section 2.5, is based on the assumption that the input strain values are periodic, and that the SNR is at least high enough to avoid that the strain values fluctuate around zero due to noise.

If these assumptions are not met, as was the case for the first clinical data set, then the elastographic processing can produce worse result than showing just strain alone. The reason for this is that the absolute value step of the elastographic processing amplifies noise. As seen in the elastographic curves from the fist clinical data set, in Fig. 4.12, the values from the noisy regions are very large. The reason that the values are so large, is because they are not included when calculating the scaling parameter β, because they have too low correlation. This also means that these extreme values can be hidden from the image by correlation coefficient thresholding.

If on the other hand the strain values have sufficient SNR and are periodic, the elastographic processing produces good images that are suitable to be displayed as a cineloop, and coul be used for real-time image. This is a big improvement from strain images, which are very difficult to interpret when displayed as a cineloop. Both the elastographic values from the second clinical data set, in Fig. 4.15, and especially from the phantom, in Fig. 4.4, illustrate the usefulness of this kind of processing.

5.3 Median filtering

It was noted in the theory chapter, section 2.6, that the median filter is very efficient in removing outliers from an image. We have never seen any issues with outliers in the axial directions at any step of our signal chain, but outliers can exist in the lateral direction. This is because the velocity

estimation is done independently for one, or possibly more depending on the lateral gate parameter, scan line. An example of such lateral discontinuities was seen in Fig. 4.5, where the lateral gate parameter was set to 1. From the same figure we see that the median filter does a good job in removing such noise, as predicted by theory. The noise removal happens without noticeably affecting spatial resolution, though this will naturally vary with the size of the median filter. A filter size of 3x3 seems to give good results on all our images.

5.4 Correlation coefficient thresholding

The correlation coefficient thresholding has been found to be a very valuable tool to identify noisy areas in the image. This is especially important when looking at the elastographic image, since as we have explained, the elastographic image can amplify noise under certain conditions. By enabling CC thresholding, this removes the possibility of not being able to separate between regions of low correlation and actual strain/elastographic values.

The CC thresholding does a good job to remove noise, as illustrated in Fig. 4.7, and since the user can control the threshold he can quickly get a feel for which of the estimates are of high quality, and which are not. The CC thresholding works well for all three data sets, as can be seen from the three elastograms, in Fig. 4.4, Fig. 4.12 and Fig. 4.15, which all have CC thresholding enabled.

5.5 Clinical findings - velocity measurements

The peak measured tissue velocity, from regions with well correlated estimates was around 0.1 mm/s for the first data set, and around 0.4 mm/s for the second data set. According to (Selbekk et al., 2005), MRI studies have found peak tissue velocities to be between 0.4 and 2.0 mm/s, depending on the study. The velocity values we found thus seem low, and there is also a big difference in peak velocity amplitude between the two data sets. However since we only measure the velocity in the direction of the ultrasound beam, the velocity estimates will vary greatly with the angle between the beam and the true velocity vector. Assuming that the two tumors were imaged at different angles, and knowing that the tumors were located in different parts of the brain, it is plausible that there could be large difference in the peak amplitude of the measured velocity. Since the MRI studies

measured the velocity vector magnitude, it is also reasonable that our axial velocity measurements will measure lower values.

The most important aspect of the velocity measurements is to determine if they are able to measure tissue movement caused by arterial pulsation. From both data sets, the velocity estimates that remained after correlation coefficient thresholding, were all found to have a periodic pattern with a fundamental frequency close to 1 Hz. The velocity curves from the two data sets, in Fig. 4.11 and Fig. 4.14, both seem to show a "spiking" pattern with a time interval of about 1 s. This pattern is quite similar to the one found from the velocity curve that was calculated from the tracking the carotid artery, shown in Fig. 3.7. In fact even the characteristic "down-up-down-up" pattern arising around the 1 s mark in the second data set, can also be seen in the carotid artery velocity curve. Further more the shape of the velocity curves, at different regions within the same data set, did not change significantly, except for regions with noise.

From these findings we feel confident that the tissue movement due to arterial pulsation in the cerebral arteries is measurable with ultrasound, and that it is the pulsation that causes the pattern seen in our velocity curves.

5.6 Clinical findings - strain measurements

If we make the simplifying, and perhaps unrealistic, assumption of linear elasticity of the tissue, we would expect the strain curves to have a shape similar to that of the velocity curves, though with more noise since we are calculating a spatial derivative.

Looking first at the filtered strain curves from data set no. 1, in Fig. 4.11, it is seen that only the strain curve from the tumorous tissue has a shape similar to the velocity curve. The tumorous strain values thus also have a periodic form. The strain in the normal tissue however, indicates compression and expansion in an almost random order, a phenomenon that arterial pulsation is unlikely to cause, there is no clear periodic pattern seen either. We believe that the strain values in the tumorous tissue could be realistic, but that the strain processing has broken down in the normal tissue, and in the noisy regions.

A possible reason for the strain processing failing for the normal tissue, could be that the tissue deformation is too small to be measured accurately. This is supported by the fact that the the peak velocity in the normal tissue was about half that of the tumorous tissue. If there is less movement there will also be less tissue deformation. We have also looked at strain curves

from other regions in the image, which are not shown, and have found that the strain processing seems to break down from all regions of the normal tissue, where the velocity is low. This break down is also seen in the strain image itself, where no realistic pattern is found. This illustrates the major challenge with pulsation based strain imaging, that we can not control the force that generates the strain and must simply hope that the pulsation force is great enough.

The strain curves from the second data set however, shown in Fig. 4.14, all have the same shape as the velocity curves. This what we expected to see, which gives us reason to believe that the measured strain values are realistic. Since the curves have similar shapes, we can compare the strain amplitudes to attempt to say something about the stiffness of the different tissue regions. We saw that there was a significant difference between the tumorous tissue (low strain), unknown tissue (medium strain) and the healthy tissue (high strain). The strain values indicate that tumor tissue is stiffer than healthy tissue, and as discussed in section 1.3 this is in agreement with other studies. Further more this indicates that strain values could be used to separate between tumor tissue and healthy tissue, which was what we hoped to see. Naturally, positive data from only one patient is not enough to confirm this, but it is nevertheless a good sign.

The strain image itself, in Fig. 4.13, shows ordered structures. From the strain image one could hypothesize that the sharp transition in strain values at the upper part of the image could represent the tumor border. If this is the case, then there is complementary information about the tumor in the strain image, compared with just using B-mode. To validate this interpretation, tissue samples would have to be gathered so that the exact tumor border could be found. This kind of histopathology has not been performed.

5.7 Clinical findings - elastographic values

The strain values from the first data set did not seem to be correct, which will naturally lead to bad results in the elastographic image as well. The performance of the elastographic processing when the strain values are of low quality has already been discussed, so we refrain from commenting on them again.

It is more interesting to look at the results from the second data set, which had more realistic strain values. We see that the elastogram and elastographic curves, as was shown in Fig. 4.15 on page 50, shows more smooth results compared with the strain curves. Especially combined with

the correlation coefficient thresholding, the elastogram gives an good indication of relative tissue stiffness, with values that are suitable for real-time display. Importantly we see that the elastographic values from the healthy tissue are higher than the values from the unknown tissue, which again are higher than the tumorous tissue values.

This elastogram could be presented to the surgeon in real-time. If indeed we can validate that there is a relationship between elastographic values and tissue pathology, this image would be of real clinical use during tumor resection.

5.8 Sources for error

We have seen contradicting results from the two clinical data sets. For one data set the strain processing appeared to break down, while for the other data set the processing worked well. A possible reason causing this difference is that we only measure strain in one dimension, when tissue deformation is in fact a multi-dimensional quantity. Our processing assumes that tissue deformation in the axial direction is always large enough to be measured, an assumption that is probably unreasonable. There might also be more than one artery that generates pulsation, further complicating the situation. The tumor location with respect to cerebral arteries and the position of the ultrasound probe with respect to the tumor will also affect the strain measurements. This makes it unreasonable to directly compare strain values between patients.

There is also a problem with the measure velocities being so small, even small movements of the probe could generate large errors in the velocity measurement. This requires that the surgeon is able to hold the probe in a fixed position, which could be a practical problem. It is not trivial to introduce a device to hold the probe in an already crowded operating room. Naturally the small amplitudes make the velocities more difficult to detect as well.

Sources for errors common to all ultrasound imaging, can naturally produce errors in the velocity and strain estimation as well. For example, side lobes in the transmit/receive beams can cause signals from structures outside the beam focus to be picked up, affecting estimation accuracy. A phenomenon which can have a potentially big negative impact on the quality of the estimates is static reverberations. Such reverberations will corrupt the velocity estimates, and can “drown” the tissue-motion signal that we are trying to measure. Static reverberations could be attempted filtered away with a high pass filter acting in the slow-time dimension. Naturally

the ever-present thermal noise in the electronics will degrade the SNR as well. All in all, the combination with the high attenuation of ultrasound waves in brain tissue, the low amplitude of the velocity signal, and the fact that we only measure quantities in one dimension seriously degrades our estimates.

CHAPTER 6

Conclusion

6.1 The estimators and MATLAB framework

We have found that the strain and elastographic estimation methods implemented seem to be well suited for imaging tissue stiffness under the presence of a low-frequency periodic and sufficiently strong force.

The least-squares based strain estimator gives improved results compared with the central-difference estimator, and is our strain estimator of choice. The correlation coefficient thresholding technique have been especially useful, and does a great job in identifying, and removing, measurements of low quality. This low quality estimate removal work well in collaboration with the elastograms.

These estimators, combined with the MATLAB framework and GUI, are not restricted to being used on the brain, and could be used for other parts of the body as well. The processing would likely work good with freehand palpation as well. This would probably require a different tuning of the parameters, but with given the GUI and the tuning guide in appendix B, this should not take long.

6.2 Clinical results

The clinical results have revealed the complexity of doing arterial pulsation based, one dimensional strain imaging. There is no guarantee that there will be enough compression of the tissue in the dimension that is being

measured, which will cause the strain processing to break down. Thus we do not believe that the strain imaging methods presented in this thesis will work on all patients.

Nevertheless, from one data set we saw strong indications that strain and elastographic values could aid in tissue segmentation. Thus for certain patients we believe that our method can have clinical usefulness.

We point out that only two clinical data sets have been studied in this thesis, and that more clinical data is needed before any certain conclusions can be made.

6.3 Suggestion for improvements and further work

First of all, more clinical data needs to be studied. Two data sets is not enough to produce any statistically significant data, and thus future work would naturally include looking at more data sets. The MATLAB GUI should allow new data sets to be studied quickly, so this is a matter of gathering more recording more clinical data.

Another way to validate the strain and elastographic measurements is by performing histopathology. The author is no expert on medical regulations, but it is likely that the results must be validated against such a "gold standard" anyway, before the method is allowed used in the operating room.

On the acquisition side, the obvious idea is to look at strain values in more than one dimensions. An easy way to quickly decide the potential usefulness of such a technique, is to do a study of the angle dependence of strain values. Doing multiple recordings from the same patient, with different angles, and studying the resulting strain values would provide such information. If it is found that the angle dependence is significant, which we suspect it is, a multi-dimensional strain estimator would most likely give better results.

A different possibility for improvement could be to make use of the electrocardiogram (ECG) signal. Since the arterial dilation is caused by the heart beating, the ECG signal could be used to time events in the heart cycle. We have seen that the strain values show a "spiking" pattern once every heart cycle, and this spike has good SNR compared with the strain values from different parts of the cardiac cycle. It is possible that by using the ECG signal to extract this spike and average the corresponding image over several cycles, a stiffness image of better quality than the elastogram could probably be produced

Another idea is to look at strain generation using some sort of external force. This would give similar imaging conditions for each patient, and avoids a lot of the problems with pulsation based strain imaging. Unfortunately the clinical effects of external deformation to the brain is unknown, so such a technique must be done with care.

Bibliography

Barber, W. D., J. W. Eberhard, and S. G. Karr (1985). A new time domain technique for velocity measurements using doppler ultrasound. *Biomedical Engineering, IEEE Transactions on 32*(3), 213–229.

Bercoff, J., M. Tanter, and M. Fink (2004). Supersonic shear imaging: a new technique for soft tissue elasticity mapping. *Ultrasonics, Ferroelectrics and Frequency Control, IEEE Transactions on 51*(4), 396–409.

Boerstad, T. (2010). Master's project: Comparison of three ultrasound velocity estimators for strain imaging of the brain. Norwegian University of Sciene and Technology.

Cespedes, E. I., C. L. de Korte, and A. F. W. van der Steen (2000). Intraluminal ultrasonic palpation: assessment of local and cross-sectional tissue stiffness. *Ultrasound in Medicine & Biology 26*(3), 385 – 396.

Cobbold, R. S. C. (2007). *Foundations of Biomedical Ultrasound*. Oxford University Press.

Dighe, M., U. Bae, M. L. Richardson, T. J. Dubinsky, S. Minoshima, and Y. Kim (2008). Differential diagnosis of thyroid nodules with us elastography using carotid artery pulsation. *Radiology 248*(2), 662–669.

Gonzales, R. C. and R. E. Woods (2008). *Digital Image Processing*. Prentice Hall.

Hall, T. J., Y. Zhu, and C. S. Spalding (2003). In vivo real-time freehand palpation imaging. *Ultrasound in Medicine & Biology 29*(3), 427 – 435.

Heimdal, A., A. Stoeylen, H. Torp, and T. Skjaerpe (1998). Real-time strain rate imaging of the left ventricle by ultrasound. *Journal of the American Society of Echocardiography 11*(11), 1013 – 1019.

Jagannathan, J., N. T. Sanghvi, L. A. Crum, C.-P. Yen, R. Medel, A. S. Dumont, J. P. Sheehan, L. Steiner, F. Jolesz, and N. F. Kassell (2009, Feb). High-intensity focused ultrasound surgery of the brain: part 1–a historical perspective with modern applications. *Neurosurgery 64*(2), 201–10.

Jensen, J. A. (1996). *Estimation of Blood Velocities Using Ultrasound*. Cambridge University Press.

Kallel, F. and J. Ophir (1997). A least-squares strain estimator for elastography. *Ultrasonic Imaging 19*(3), 195–208.

Loupas, T., J. Powers, and R. Gill (1995, jul.). An axial velocity estimator for ultrasound blood flow imaging, based on a full evaluation of the doppler equation by means of a two-dimensional autocorrelation approach. *Ultrasonics, Ferroelectrics and Frequency Control, IEEE Transactions on 42*(4), 672 –688.

Mace, E., I. Cohen, G. Montaldo, R. Miles, M. Fink, and M. Tanter (2011). In vivo mapping of brain elasticity in small animals using shear wave imaging. *IEEE Trans Med Imaging 30*(3), 550–558.

Markus, H. S. (2000). Transcranial doppler ultrasound. *British Medical Bulletin 56*, 378.

McKnight, A. L., J. L. Kugel, P. J. Rossman, A. Manduca, L. C. Hartmann, and R. L. Ehman (2002). Mr elastography of breast cancer: Preliminary results. *Am. J. Roentgenol. 178*(6), 1411–1417.

Meyer-Wiethe, K., F. Sallustio, and R. Kern (2009). Diagnosis of intracerebral hemorrhage with transcranial ultrasound. *Cerebrovasc Dis 27 Suppl 2*, 40–47.

Miller, K. and K. Chinzei (1997). Constitutive modelling of brain tissue: Experiment and theory. *Journal of Biomechanics 30*(11-12), 1115 – 1121.

Miller, K. and K. Chinzei (2002). Mechanical properties of brain tissue in tension. *Journal of Biomechanics 35*(4), 483 – 490.

Nightingale, K., M. S. Soo, R. Nightingale, and G. Trahey (2002). Acoustic radiation force impulse imaging: in vivo demonstration of clinical feasibility. *Ultrasound in Medicine & Biology 28*(2), 227 – 235.

Ophir, J., S. K. Alam, B. Garra, F. Kallel, E. Konofagou, T. Krouskop, and T. Varghese (1999). Elastography: ultrasonic estimation and imaging of the elastic properties of tissues. In *In Proc. Instn. Mech. Engrs., Part H: Journal of Engineering in Medicine*, pp. 203–233.

Ophir, J., I. Cspedes, H. Ponnekanti, Y. Yazdi, and X. Li (1991, Apr). Elastography: a quantitative method for imaging the elasticity of biological tissues. *Ultrason Imaging 13*(2), 111–134.

Pesavento, A., A. Lorenz, S. Siebers, and H. Ermert (2000). New real-time strain imaging concepts using diagnostic ultrasound. *Physics in Medicine and Biology 45*(6), 1423.

Rygh, O. M. (2008). *3D ultrasound based neuronavigation in neurosurgery.* Ph. D. thesis, Norwegian University of Science and Technology, Faculty of medicine, Department of Neurosciene.

Scholz, M., A. Lorenz, A. Pesavento, B. Brendel, W. Khaled, M. Engelhardt, I. Pechlivanis, V. Noack, A. Harders, and K. Schmieder (2007, Oct). Current status of intraoperative real-time vibrography in neurosurgery. *Ultraschall Med 28*(5), 493–497.

Scholz, M., V. Noack, I. Pechlivanis, M. Engelhardt, B. Fricke, U. Linstedt, B. Brendel, D. Ing, K. Schmieder, H. Ermert, and A. Harders (2005, Jul). Vibrography during tumor neurosurgery. *J Ultrasound Med 24*(7), 985–992.

Selbekk, T., J. Bang, and G. Unsgaard (2005, Jan). Strain processing of intraoperative ultrasound images of brain tumours: initial results. *Ultrasound Med Biol 31*(1), 45–51.

Selbekk, T., R. Brekken, O. Solheim, S. Lydersen, T. A. N. Hernes, and G. Unsgaard (2010, Jan). Tissue motion and strain in the human brain assessed by intraoperative ultrasound in glioma patients. *Ultrasound Med Biol 36*(1), 2–10.

Shiina, T., M. Yamakawa, N. Nitta, E. Ueno, T. Matsumura, S. Tamano, and T. Mitake (2003). Clinical assessment of real-time, freehand elasticity imaging system based on the combined autocorrelation method. In *Proc. IEEE Symp. Ultrasonics*, Volume 1, pp. 664–667.

Solheim, O., T. Selbekk, A. Jakola, and G. Unsgrd (2010). Ultrasound-guided operations in unselected high-grade gliomasoverall results, impact of image quality and patient selection. *Acta Neurochirurgica 152*, 1873–1886.

Souchon, R., O. Rouvire, A. Gelet, V. Detti, S. Srinivasan, J. Ophir, and J.-Y. Chapelon (2003). Visualisation of hifu lesions using elastography of the human prostate in vivo: preliminary results. *Ultrasound in Medicine & Biology 29*(7), 1007 – 1015.

Sugawara, M., K. Niki, H. Furuhata, S. Ohnishi, and S. Suzuki (2000). Relationship between the pressure and diameter of the carotid artery in humans. *Heart Vessels 15*(1), 49–51.

Uff, C., L. Garcia, J. Fromageau, N. Dorward, and J. Bamber (2009, sept.). Real-time ultrasound elastography in neurosurgery. In *Ultrasonics Symposium (IUS), 2009 IEEE International*, pp. 467 –470.

APPENDIX A

Source code and implementation details

The AC function

To implement Eq. (2.3) efficiently on a set of RF frames can be challenging, but by using built-in MATLAB functions it can be calculated elegantly. The autocorrelation function is only needed for three different lags, but for all spatial locations. The three lags needed are $\gamma[0,0]$, $\gamma[0,1]$ and $\gamma[1,0]$. Only autocorrelation estimates which have a full range and lateral gate are kept, this is enforced by providing the '*valid*' option to the convolution function in MATLAB.

We let the input be a set of RF frames, where the number of frames is the ensemble length **O**. The frames are stacked in a three-dimensional matrix X representing the signal $x_+[m,n,o]$. The code provided below calculates the three values of the autocorrelation function at all spatial locations, and stores the results as three matrices. Note that the code consists only of matrix calculations and built-in functions, avoiding loops which can often suffer from performance penalties in an interpreted langue like MATLAB.

```
1 % gamma[0,1]. Note that the last row of X is ignored, so ...
      that gamma[0,1] and gamma[1,0] have the same dimensions.
2 gamma_0_1 = X(1:end-1,:,1:end-1).*conj(X(1:end-1,:,2:end));
3
4 % The third dimension is the ensemble length
5 gamma_0_1 = sum(gamma_0_1, 3);
6
```

```
% The range gate and lateral gate computations can be ...
    solved using convolution
gamma_0_1 = conv2(gamma_0_1, ones(U,1), 'valid');
gamma_0_1 = conv2(gamma_0_1, ones(1,V), 'valid');

% Note that the two convolutions above could be ...
    expressed as a single 2D convolution with the kernel ...
    ones(U,V). However since ones(U,V) is a separable ...
    kernel, it is faster to perform two 1D convolutions ...
    instead.

% Same procedure for gamma[1,0]
gamma_1_0 = X(1:end-1,:,:).*conj(X(2:end,:,:));
gamma_1_0 = sum(gamma_1_0, 3);
gamma_1_0 = conv2(gamma_1_0, ones(U,1), 'valid');
gamma_1_0 = conv2(gamma_1_0, ones(1,V), 'valid');



% And for gamma[0,0]. Again ignoring the last row
% to keep the same dimensions as the other matrices
gamma_0_0 = X(1:end-1,:,:).*X_conj(1:end-1,:,:)
gamma_0_0 = sum(gamma_0_0,3);
gamma_0_0 = conv2(gamma_0_0, ones(U,1), 'valid');
gamma_0_0 = conv2(gamma_0_0, ones(1,V), 'valid');
```

Central-difference strain estimation

We see that Eq. (2.17) can be represented as a convolution between $\hat{V}[m,n]$ and the row-vector h with $\Delta m + 1$ rows defined by:

$$h(n) = \begin{cases} \kappa/\Delta m & \text{if } n = 0, \\ -\kappa/\Delta m & \text{if } n = \Delta m, \\ 0 & \text{otherwise.} \end{cases}$$

Given the vector $h(n)$ above, it is trivial to implement the central-difference estimator by convolution in MATLAB:

```
h           = zeros(dlta_m + 1,1);
h(1)        = kappa/dlta_m;
h(dlta_m+1) = -kappa/dlta_m;
S           = conv2(V,h,'valid');
```

Least-squares strain estimation

MATLAB has many built-in functions to find least-squares solutions to linear systems, examples are the backslash operator "\", the function *lscov* or the function *pinv*. A naive implementation is to iterate through the entire velocity matrix and apply one of these functions to each axial segment, solving Eq. (2.21) for each segment. For a velocity matrix of size 1000 by 128 this approach takes about 5 seconds, and can not be used for real-time imaging. Fortunately, since only the slope of the straight line, and not the offset, is needed, the least-squares solution can be found with convolution.

This is seen by first assuming that Δm is chosen such that *all* the velocity estimates will be used in strain estimation. We let the number of velocity estimates be n, which means that $\Delta m = n + 1$. The matrix $\mathbf{A}$ in eq. (2.20) becomes:

$$\mathbf{A} = \begin{bmatrix} 1 & 1 \\ 2 & 1 \\ \vdots & \vdots \\ n & 1 \end{bmatrix}$$

Then the matrix $\left[\mathbf{A}^T\mathbf{A}\right]^{-1}\mathbf{A}^T$ in (2.21) is needed, and is found by first calculating:

$$\begin{aligned} \mathbf{A}^T\mathbf{A} &= \begin{bmatrix} 1 & 2 & \cdots & n \\ 1 & 1 & \cdots & 1 \end{bmatrix} \begin{bmatrix} 1 & 1 \\ 2 & 1 \\ \vdots & \vdots \\ n & 1 \end{bmatrix} \\ &= \begin{bmatrix} \frac{n(n+1)(2n+1)}{6} & \frac{n(n+1)}{2} \\ \frac{n(n+1)}{2} & n \end{bmatrix} \end{aligned}$$

The inverse is found by using the general inverse rule for a 2x2 matrix:

$$\begin{aligned} \left[\mathbf{A}^T\mathbf{A}\right]^{-1} &= \frac{12}{n(n^2-1)} \begin{bmatrix} 1 & -\frac{n+1}{2} \\ -\frac{n+1}{2} & \frac{(n+1)(2n+1)}{6} \end{bmatrix} \\ &= a(n) \begin{bmatrix} 1 & -\frac{n+1}{2} \\ -\frac{n+1}{2} & \frac{(n+1)(2n+1)}{6} \end{bmatrix} \end{aligned}$$

Only the first row of $\left[\mathbf{A}^T\mathbf{A}\right]^{-1}\mathbf{A}^T$ is needed, since this is the row that is

involved in calculating $\hat{a}$. The first row of $\left[\mathbf{A}^T\mathbf{A}\right]^{-1}\mathbf{A}^T$ is a vector $h(n)$:

$$\begin{aligned} h(n) &= a(n)\left[1, \quad -\tfrac{n+1}{2}\right]\begin{bmatrix} 1 & 2 & \cdots & n \\ 1 & 1 & \cdots & 1 \end{bmatrix} \\ &= a(n)\left(\begin{bmatrix} 1 & 2 & \cdots & n \end{bmatrix} - \begin{bmatrix} \frac{n+1}{2} & \frac{n+1}{2} & \cdots & \frac{n+1}{2} \end{bmatrix}\right) \end{aligned}$$

which is equivalent to:

$$h = \kappa\frac{12}{n(n^2-1)}\left(\begin{bmatrix} n & n-1 & \ldots & 1 \end{bmatrix} - \begin{bmatrix} \frac{n+1}{2} & \frac{n+1}{2} & \cdots & \frac{n+1}{2} \end{bmatrix}\right)^T$$

By convolving this vector with the velocity matrix, the least-squares solution is found for the axial length $\Delta m = n - 1$.

The following MATLAB code, where V is the velocity matrix, calculates the strain matrix in around 0.01 seconds, a significant speed-up compared with the 5 seconds it took with the naive implementation. This shows the importance of avoiding for-loops and using only built-in functions when optimizing for speed in MATLAB.

```
1 h   = kappa * 12/(n*(n^2-1)) * ( (n:-1:1) - (n+1)/2 )';
2 S   = conv2(V,h,'valid');
```

Adaptive scaling

Letting *frame* be the input frame, *cFrame* be the correlation coefficient matrix, the following MATLAB code implements the adaptive scaling:

```
1 thr = 0.9;   % Corr. coefficient threshold (set in GUI)
2 tol = 0.98;  % The percentage of pixels that are to be ...
      bounded
3 cFrame(cFrame > thr)   = 1;
4 cFrame(cFrame <= thr) = 0;
5 bounds = stretchlim(c2.*frame, [0, tol]);
6 frame  = frame./bounds(2);
```

where *stretchlim* is a function which comes with the image processing toolbox, that finds the upper bound that *tol* % of the matrix elements are below.

APPENDIX B

How to tune parameters

The tuning of estimation parameters is always a question of trade-offs, and the trade-off is usually a choice between noise and spatial resolution. The guide presented here is the way the parameters have been tuned for all data sets in this thesis, a tuning which can be performed quickly using the GUI. This is an ad hoc method, and is not guaranteed to give optimal parameters, but we have found that it gives images that are "optimal enough" in some sense.

The easiest way to understand what each parameter effects, is simply to play around with the values in the GUI, and observing the effect on the image. Doing this, one quickly gets a "feel" for what parameters do and how they influence each other.

The idea behind this procedure is easy. Start by having the parameters optimized for spatial and temporal resolution as possible. This will correspondingly give an extremely noisy image. Then optimize for one dimension at a time (axial, lateral, temporal), by increasing the corresponding parameters, until the noise is at an acceptable level. We have found that it is better to have some noise, than to risk missing information due to poor resolution. Keep in mind that the values suggested here must be changed if the acquisition parameters are different from the ones we use.

Procedure:

1. **Velocity parameters**. Start by having both the velocity and strain image visible, so the effects can be easily seen. Set the range gate equal to the length of the transmitted pulse (usually somewhere around 10 samples), lateral gate to 1 and ensemble length 2. Increase the lateral gate until lateral noise seems to be at an acceptable level. A value less

than 6 is usually sufficient. We have not found that any improvements by increasing the ensemble length, though it is likely that this could have an effect if the FPS (which in practice is the PRF in our case), is very high.

Now investigate the velocity and strain frames from different points in time by moving the slider. If the values jump up and down, enable the low pass filter with a low order. Keep increasing the order until the image looks good for most or all frames.

2. **Strain parameters**. We recommend to always use the LSQ estimator. By looking only at the strain image, increase the axial length from 2 samples and up to a maximum of about 100, in steps of ten or so. Pay attention to structures in the image, if they start to "wash out", the axial length is too long and should be reduced.

3. **Elastographic parameters**. Enable the elastographic window to observe the effects. Pick a frame where there is little strain. If the elastographic image looks good for this frame, it will also look good for frames where there is a strong strain signal. Increase the LPF order until you are satisfied with the result, but be reasonable. The correlation parameter is set the same as the one used for correlation coefficient thresholding, explained next.

4. **Post-processing**. The median filter can be enabled if there is a lot of noise, though this is usually not necessary. The filter usually produces a nicer image, so we usually keep it enabled. Enable the correlation coefficient with a low coefficient, say 0.6. Keep increasing it in steps of say 0.1, until the noisy areas are gone. A value of 0.7 to 0.95 usually gives good results.

APPENDIX C

Acquisition and algorithmic parameters

This appendix shows the acquisition parameters that were used during recording of the three data sets. In addition to this, the algorithmic parameters used to produce all the figures from the "Results" chapter is given. N/A means not applicable, meaning that the parameter is not available, not involved or not relevant to the figure in question. Remember that the effect of most of the algorithmic values will change with acquisition parameters as well. For example a range gate of 30 samples represents a different physical range at 10 MHz sampling frequency than at 20 MHz sampling frequency.

Table C.1: Acquisition parameters from the three data set

	Phantom	Data set 1 (2011)	Data set 2 (2004)
System	SonixMDP	SonixMDP	System FiVe
Probe	FLA 5–14 MHz	FLA 5–14 MHz	FLA 10-MHz
Transmit freq	10 MHz	5 MHz	8 MHz
RF sampling freq	20 MHz	20 MHz	20 MHz
No. scan lines	128	96	174
No. depth samples	1032	1304	776
Height x Depth	N/A	50x28 mm	30x32 mm
No. frames	194	290	79
FPS	49	58	46.2

Table C.2: Algorithmic parameters used - 1 of 3

	Fig. 4.1, Fig. 4.4 Fig. 4.2	Fig. 4.7	Fig. 4.11 Fig. 4.12
Data set	Phantom	Phantom	Data set 1 (2011)
Velocity estimation			
Estimator	2D-AC	2D-AC	2D-AC
Range gate (**M**)	6 samples	6 samples	30 samples
Lateral gate (**N**)	3 lines	3 lines	5 lines
Ensemble length (**O**)	2 frames	2 frames	2 frames
LPF order	4	N/A	15
LPF cut-off freq	2 Hz	N/A	2 Hz
Strain estimation			
Estimator	LSQ	LSQ	LSQ
Axial length (Δm)	90 samples	90 samples	70 samples
Elasto. processing			
LPF order	10	3	10
LPF cut-off freq	2 Hz	2 Hz	2 Hz
Post processing			
Median filter (axial x lateral)	3x3	N/A	3x3
Correlation thresholding	Fig. 4.1: Off. Fig. 4.2: Off Fig. 4.4: 0.95	N/A	0.95

Table C.3: Algorithmic parameters used - 2 of 3

	Fig. 4.8 Fig. 4.10 Fig. 4.9,	Fig. 4.6	Fig. 4.5
Data set	Data set 1 (2011)	Phantom	Phantom
Velocity estimation			
Estimator	2D-AC	2D-AC	2D-AC
Range gate (**M**)	30 samples	6 samples	15 samples
Lateral gate (**N**)	5 lines	3 lines	1 lines
Ensemble length (**O**)	2 frames	2 frames	2 frames
LPF order	N/A	N/A	4
LPF cut-off freq	N/A	N/A	2 Hz
Strain estimation			
Estimator	LSQ	N/A	LSQ
Axial length (Δm)	70 samples	N/A	70 samples
Post processing			
Median filter (axial x lateral)	3x3	N/A	N/A
Correlation thresholding	N/A	N/A	N/A

Table C.4: Algorithmic parameters used - 3 of 3

	Fig. 4.13 Fig. 4.14 Fig. 4.15,
Data set	Data set 2 (2004)
Velocity estimation	
Estimator	2D-AC
Range gate	20 samples
Lateral gate	3 lines
Ensemble length	2 frames
LPF order	N/A
LPF cut-off freq	N/A
Strain estimation	
Estimator	LSQ
Axial length	60 samples
Elasto. processing	
LPF order	10
LPF cut-off freq	2 Hz
Post processing	
Median filter (axial x lateral)	3x3
Correlation thresholding	0.98